Ultra-high temperature shape memory behavior in Ni-Ti-Hf alloys

O. Benafan[a,*] G.S. Bigelow[a], A. Garg[b,a], L.G. Wilson[a], R.B. Rogers[a], E.J. Young-Dohe[a], D.F. Johnson[a], D.A. Scheiman[c,a], J.W. Lawson[d], and Zhigang Wu[d]

[a]Materials and Structures Division, NASA Glenn Research Center, Cleveland, OH 44135, USA
[b]University of Toledo, Toledo, OH 43606, USA
[c]Universities Space Research Association, 7178 Columbia Gateway Drive, Columbia, MD, 21046, USA
[d]Intelligent Systems Division, NASA Ames Research Center, Moffett Field, California 94035, USA

*Corresponding author: Tel.: +1 (216) 433-8538; fax: +1 (216) 977-7132.
E-mail address: othmane.benafan@nasa.gov (O. Benafan).

Abstract

Shape memory behavior in stoichiometric Ni-Hf-Ti shape memory alloys with high Hf was evaluated. Five alloy compositions with a hafnium content from 30 to 50 at.% were arc melted, homogenized and tested to reveal microstructure and shape memory properties. Transformation temperatures increased linearly with Hf addition, reaching a maximum austenite finish temperature of 1190 °C at 50Hf, measured using differential scanning calorimetry (DSC). The low temperature stable microstructures were composed of a majority B33 orthorhombic phase, with traces of B19′ monoclinic structure below the martensite finish temperature, as revealed by X-ray diffraction (XRD) and Transmission Electron Microscopy (TEM). These microstructures convert to a B2 cubic structure at higher temperature. Macroscopically, specimens were tested isothermally at room temperature, and endured stresses as high as 1 GPa in compression. Strain recovery decreased from nearly 100% recovery in the 30Hf alloy, to nearly 0% at 50Hf alloy, as plasticity mechanisms dominated at high temperatures in the higher Hf alloys. Uniaxial constant-force thermal cycling (UCFTC) experiments revealed limited work output at high temperatures due to creep-dominant mechanisms simultaneously occurring during the phase transformation process.

Keywords: NiHfTi; High-temperature shape memory alloy; Martensitic transformation; B33.

1. Introduction

Hafnium (Hf) addition to the NiTi-based alloys is known to increase the phase transformation temperatures, resulting in viable shape memory alloys (SMA) for high temperature actuator applications. Research and development of these NiTiHf alloys progressed from fundamental studies to large-scale production and prototyping in the NiTi-20Hf at.%, which has been the most studied and utilized formulation. This NiTi-20Hf alloy exhibits transformation temperatures as high as 330 °C, depending on the Ni content, while still being amenable to processing into useful forms (e.g., rods and sheets) [1]. However, there is a need for higher activation temperatures to satisfy warmer systems in aeronautics (e.g., engine related applications, supersonic inlets, hypersonic skin morphing), space applications (e.g., solar orbiters, Venus probes), and potential uses in other fields. Limited means of achieving this capability exist – current solutions include more expensive systems such as TiPt [2] or RuNb [3] alloys, or recently examined multi-component alloys [4]. As an alternative, building from the authors' previous success on the lower Hf alloy (NiTi-20Hf at.%) [1], higher ternary Hf additions between 30-50Hf were explored to assess this goal.

Previous studies have explored alloys with compositions up to 30 at.% Hf. Early work by AbuJudom et al. [5] and Angst et al. [6] reported on Ti-rich NiTiHf arc melted buttons with 25 and 30 at.% Hf, demonstrating that the latter alloy composition can reach an austenite peak temperature (A_p) of 622 °C. Pu et al. [7], Zhu et al. [8] and Wu et al. [9] reported on Ti-rich vacuum induction-melted ingots and sheets with Hf content as high as 30 at.%, and showed the highest A_p temperature to be 444 °C. Potapov et al. [10] examined melt spun $Ni_{49.8}Ti_{25.2}Hf_{25}$ at.% ribbons and did not observe a transition up to the test temperature of 350 °C. Gu et al. [11] reported on pulsed laser deposited $Ni_{49.4}Ti_{20.7}Hf_{29.9}$ (at.%) thin films and showed an A_p

temperature of 228 °C, which is much lower than the previously reported values. In addition to the slight composition dissimilarities, these temperature differences among materials with relatively similar Hf contents can likely be attributed to the alloys' production methods and their resulting microstructural disparities. Kang and Nam [12] plasma melted a stoichiometric $Ni_{50}Ti_{20}Hf_{30}$ (at.%) and performed crystal structure studies by means of transmission electron microscopy (TEM) and X-ray diffraction (XRD). Sanjabi et al. [13, 14] used DC magnetron sputtering to produce NiTiHf films, where the higher Hf composition produced was $Ni_{49.2}Ti_{22.1}Hf_{28.7}$ (at.%). The authors reported signal noise during differential scanning calorimetry (DSC) measurements, preventing them from determining transformation temperatures for this composition. However, they were able to measure transition temperatures of an alloy with reduced Hf – $Ni_{49.3}Ti_{26.3}Hf_{24.4}$ – finding an A_p temperature of 414 °C. Using a similar production technique, Tong et al. [15] produced a $Ni_{45}Ti_{32}Hf_{23}$ (at.%) alloy with an approximate A_p temperature of 280 °C, in the annealed condition. Rao et al. [16] also examined thin films with a composition of $Ni_{40}Ti_{30}Hf_{30}$ (at.%) and measured an A_p temperature of 153 °C, which is lower than previous studies, but note that the Ni/Ti/Hf ratios are not identical. While all the aforementioned alloys in the Hf range above 20% were Ti-rich (Ti+Hf >50 at.%) or stoichiometric (Ti+Hf =50 at.%), Santamarta et al. [17] first reported on a slightly Ni-rich $Ni_{50.1}Ti_{24.9}Hf_{25}$ (at.%) alloy (Ti+Hf <50 at.%) produced using vacuum induction melting. In their work, the authors studied precipitates that form in this alloy using ab initio density functional theory (DFT) calculations and TEM. Continuing with a Ni-rich composition, Patriarca et al. studied alloys with near 25 at.% Hf in a polycrystal aggregate [18] and in a single crystal form [19-21], and showed an A_p temperature between 200 and 350 °C depending on the aging heat treatments. Bucsek et al. [22] examined a $Ni_{50.3}Ti_{25.6}Hf_{24.1}$ (at.%) alloy, with an austenite

finish temperature (A_f) of approximately 291 °C. Recently, Umale et al. [23] examined several arc melted buttons with varying Ni content up to 51 at.% and with Hf addition up to 30 at.%, and the study showed an A_f temperature as high as 620 °C depending on the Ni content. A summary of all these works with additional details is listed in Table 1.

These previous studies mentioned above elucidated the high temperature potential of NiTiHf alloys up to 30 at.%, but there are no reports of transformation temperature and shape recovery for higher Hf additions. Moreover, there exist several discrepancies around what phases and crystal structures exist in alloys with over 20 at.% Hf, and whether there is a martensitic transformation and shape memory behavior in compositions with Hf content above 30 at.%. It has been established that the high temperature phase is a cubic (B2) phase, but the lower temperature phases reported vary depending on the Hf content. For NiTiHf alloys with Hf content below 20 at.%, there is consistent reporting of a transformation path from a cubic to monoclinic structure (B2→B19′) on cooling. In the range between 20 and 30 at.%, there are mixed reports regarding transformation paths; (Cubic B2→Monoclinic B19′) [10, 23], (Cubic B2→Orthorhombic B19) [7, 9, 18], (Cubic B2→Rhombohedral R-phase) [16], or a combination thereof [12, 21]. For Hf content above 30 at.%, it is consistently reported that the transformation path progresses via a B2 to an orthorhombic CrB-Type (B33) structure as identified by a pseudo-binary phase diagram developed by Yeremenko et al. [24] and others [25-27], and phase equilibria studies performed by Semenova et al. [28] and Ross et al. [29]. The only other stable phase reported in this range is an unknown ternary phase, termed "τ", that was found at 800 and 900 °C [30].

With this historical context in mind, to the best of our knowledge, there are no reports of martensitic transformation temperatures in the NiTiHf alloys with Hf above 30 at.%. Nor is there

any evidence of shape memory behavior with reversible dimensional changes in these alloys. Thus, it is the goal of this work to study these properties in the NiTi-(30-50 at.% Hf) alloy compositional range. In particular, the thermomechanical responses were evaluated using DSC, uniaxial prestrain and free recovery (UPFR), and uniaxial constant force thermal cycling (UCFTC). Microstructural assessments were conducted using XRD, scanning electron microscopy (SEM), and TEM. Computational methods based on *ab initio* simulations were also used to predict martensitic transitions in these NiTiHf alloys and provide additional insights into complementary phase stabilities. Furthermore, the availability of experimental data helps benchmark these first-principles methods on their applicability to complicated ternary SMAs.

2. Experimental Methods

Experimental alloys with a target composition of $Ni_{50}Hf_XTi_{50-X}$ (X = 30, 35, 40, 45, and 50 at.%), were produced by vacuum, non-consumable-arc melting of high purity constituents using a water cooled copper crucible. Buttons of 30 grams were melted and re-melted five times under an argon atmosphere to ensure complete mixing and homogeneity. Each button was then weighed and compared to the charge weight (before melting) to confirm negligible or no loss of alloying materials during the melting process. All buttons were weighed to be within 30 ± 0.01g. Buttons were then suction cast into 5 mm diameter rods using a copper mold. The suction cast rods and remaining hot-tops were homogenized in vacuum for 24 hours at 1050 °C followed by argon gas quenching.

Cylindrical test specimens were machined from the ingots using wire electrical discharge machining (EDM). Cylinders were centerless ground to 5mm diameters, and the flat ends were hand polished to remove any recast layers and attain an appropriate parallelism between the two surfaces.

DSC measurements were conducted using a NETZSCH 404 F1 Pegasus® – High-Temperature DSC equipped with a rhodium furnace. Specimens, 5 mm in diameter by 1 mm thick, were thermally cycled three times from room temperature and up to 1350 °C under argon gas and in vacuum using heating and cooling rates of 10 °C/min.

Microstructures were examined using a Thermo Fisher Talos Scanning/Transmission Electron Microscope, F200 (S/TEM). TEM specimens consisted of 3 mm diameter disks that were mechanically ground to a thickness of ≈130 μm, followed by electropolishing using a solution of 20% H_2SO_4 and 80% methanol (by volume) cooled to -5 °C in a Struers Tenupol-5 twin-jet electropolisher. TEM microstructure data were recorded at room temperature, below the martensite finish temperature. SEM was also performed at room temperature using a Hitachi 4700 microscope. Samples were mounted, polished, and etched using a solution of 10% HF, 40% HNO_3, and 50% H_2O (by volume) for general SEM examination. The Electron Back Scattered Diffraction (EBSD) with simultaneous Energy Dispersive Spectroscopy (EDS) was performed on a TESCAN MAIA3 Field Emission Scanning Electron Microscope (FE-SEM). The crystallographic data were collected, and phase analysis was carried out.

XRD scans were collected using 5mm diameter disks from the homogenized suction cast rods and using larger area sections from the homogenized button hot-tops. Before scanning, samples were polished and ultrasonically cleaned. Given the nature of the samples and the relatively large grain morphology associated with as-cast materials, both 1D and 2D diffraction patterns were acquired from multiple samples and repeated melts to confirm phase identification. All XRD scans were collected with Cu Kα radiation using Bragg-Brentano geometry. One-dimensional (1D) scans on the buttons were collected using a Bruker D8 Advance diffractometer with variable slits, 0.02-degree step size, 2.5 seconds per step scan speed, and 10-80 degrees 2-

theta scan range. One-dimensional (1D) scans on the smaller, suction cast material were conducted on a Malvern PANalytical Empyrean diffractometer using point focus mode and fixed crossed slits to accommodate the small sample size, with a 0.04-degree step size, 0.2 degrees per second scan speed, and 10-120 degrees 2-theta scan range. Two-dimensional 2D XRD scans were collected on a Bruker D8 Discover diffractometer with General Area Diffraction Detector System, 240 second per frame scan speed, 10-120 degrees 2-theta scan range, and integrated to 0.02-degree step size. Whole pattern fitting refinements were performed using MDI Jade (Materials Data Inc., Version 8.7). Both structure (Rietveld) and structureless refinements were performed, with freedom in lattice constant, preferred orientation, and structure factor.

Thermomechanical tests were performed using an MTS 810 servo-hydraulic load frame. Specimens, 5 mm in diameter and 10 mm long, were mounted on the load frame using two ME3 superalloy platens to apply compressive loads. Heating was performed using an Ameritherm NovaStar 7.5kw induction heater, whereas temperature was controlled and measured using a Eurotherm 3504 controller and type K thermocouples. Macroscopic strains were measured using a Micro-Epsilon optoControl 2600 LED micrometer. Two types of tests were performed: The first consisted of series UCFTC tests at different stress levels, following a modified E3097 ASTM test method [31]. In these tests, samples were loaded at room temperature to stresses between 0 and 200 MPa in compression. Samples were then heated to an upper cycle temperature (UCT) above the austenite finish and cooled to a lower cycle temperature (LCT) below the martensite finish temperature. This procedure was performed twice at each different stress level, and the 2^{nd} thermomechanical cycle is reported here (noting that the loading to a designated stress was performed at room temperature martensite, the 1^{st} cycle is not reported due to the initial martensite reorientation process, whereas the 2^{nd} cycle represents the full complete

heating and cooling segments, as habitually done when reporting SMA actuation data). The second set of experiments consisted of isothermal deformation at room temperature following the UPFR procedure outlined in the ASTM E3098 standard test method [32]. In this work, samples were deformed to -1 GPa and then unloaded to 0 GPa in strain control using a strain rate of 1×10^{-4} s^{-1}. Due to the limited heating capability in the servohydraulic test frame, samples were moved to a dilatometer, where the stress-free thermal recovery was performed.

A Netzsch DIL 402C dilatometer was used for these measurements under helium atmosphere, with a flow rate of 50 cm^3/min. Heating and cooling rates of 5 °C/min were used between room temperature and the prescribed maximum temperature for each alloy composition, with 10 min isothermal holds at each temperature extreme for system equilibration. The dilatometer pushrod contact force was set at a standard 0.3 N. Each sample was thermally cycled 3 times through the phase transition region to observe the strain recovery if any. The first heating cycle served to determine the strain recovery post unloading, while the successive cycles were used to observe the simple volume distortion and the associated strain recovery, representative of a two-way shape memory effect (TWSME).

3. Computational Methods

To determine the phase transitions in the $Ni_{50}Ti_{50-x}Hf_x$ ternaries, the Gibbs free energies (G) were calculated as a function of temperature in the B2, B19', and B33 phases at x = 25, 31.25, 37.5, 43.75, and 50 at.%. Each structure was generated using the special quasi-random structures (SQS [33, 34]) method. Specifically, SQS 48-atom unit cells were used for these NiTiHf ternaries, containing 12, 15, 18, 21, and 24 Hf atoms, respectively. The phase designations B2, B19', and B33 correspond to cubic (CsCl-type), monoclinic (the monoclinic angle is fixed at 98°), and orthorhombic (CrB-type) lattices. While atomic positions in the reference structures of

the B19' and B33 phases were relaxed, the internal coordinates of the reference structure of the B2 phase were obtained by averaging 25,000 (50 ps) snapshots at high temperatures using the *ab initio* molecular dynamics (AIMD) simulations.

The calculations of total energy and lattice vibrations and the AIMD simulations were carried out using the VASP package [35-38]. The Perdew, Burke, and Ernzerhof (PBE) [39] density functional and the projector augmented wave method (PAW [40, 41]) were used in DFT calculations. The valence ground states of Ni, Ti and Hf atoms include $3d^9 4s^1$, $3d^2 4s^2$, and $5d^2 6s^2$ electrons, respectively.

The Gibbs free energy *G* can be expressed as

$$G(T) = E[V(T)] + F^{el}(T) + F_h^{ph}(T) + F_{anh}^{ph}(T).$$

Here *E* is the total electronic energy for the reference structure, whose volume (*V*) is optimized at temperature *T*. The remaining three terms, F^{el}, F_h^{ph} and F_{anh}^{ph}, are the electronic free energy, and the harmonic and anharmonic parts of the phonon free energy, respectively. Lattice vibrations, AIMD simulations and thermodynamics integration were carried out to evaluate the vibrational free energy contributions to *G*. Technical details can be found in Ref. [42].

4. Results and Discussion

4.1 Thermal Analysis

Thermal analysis results obtained using DSC are shown in Fig. 1. For better visualization, the data were vertically offset, and only the 2nd and 5th cycles are plotted. The DSC thermograms show transformation peaks on heating and on cooling, commensurate with the typical martensitic transformation in NiTiHf alloy system. Several key observations can be made from these plots. First, transition peaks shift to higher temperatures with the addition of Hf, and the majority of the

peaks are asymmetric in nature, seldom exhibiting multiple overlapping peaks. Second, large thermal hysteresis is observed associated with the forward and reverse transition. Hysteresis in this case is calculated as the austenite finish temperature minus the martensite start temperature (A_f - M_s), which were extracted and labeled following conventional SMA data parsing procedures [43]. During thermal cycling, transformation enthalpies decrease, mainly in the lower Hf containing alloys, up to the tested 5th cycle, while changes in transformation temperatures were negligible. While this thermal instability is commonly detected in fully annealed materials and in alloys with no precipitation or solid solution strengthening, it appears that oxidation may also play a role. DSC tests were performed under vacuum and under argon backfill atmosphere to eliminate or reduce oxide formation. This was successful for impeding severe oxide formation, but after visual inspection, the samples still displayed a slight discoloration, indicating an oxide layer. To magnify the potential effect of oxides, given the practical use of these alloys will most likely be in open air, new DSC samples were tested under argon flow alone with no vacuum. An example of the resulting peak evolution is shown in Fig. 2 for the NiTi-30Hf alloy. Clearly, a new peak around 1175 °C appears and intensifies with thermal cycling. Concurrently, the enthalpy peaks associated with the matrix martensite-to-austenite transformation around 600 °C decrease in intensity. This new peak is associated with the monoclinic-to-tetragonal phase transformation in HfO_2 as reported elsewhere [44]. As the HfO_2 fraction increases with cycling, there is less volume faction of the base material that undergoes the martensitic transformation, hence lower enthalpy peaks are seen relative to previous cycles. Keeping in mind that HfO_2 plays a role, the thermal instability shown in Fig. 1 is mainly attributed to typical effects associated with “untrained” materials, given the alloys considered here were only homogenized without any additional heat treatments or secondary processing.

The measured characteristic temperatures are plotted as a function of Hf content in Fig. 3 and listed in Table 2. For reference, the phase boundary lines adopted from Yeremenko et al. [24] are plotted, along with the reported crystal structures δ_1 (CsCl-type) and δ_2 (CrB-type). Noting that δ_1 is equivalent to B2 and δ_2 is equivalent to B33 phase designation. Adding Hf resulted in a quantitatively linear increase in transition temperatures up to the 50Hf alloy. This is in line with the quasilinear relationship obtained in alloys with a Hf content between 15 and 30 at.% as shown by several reports [6, 23]. In reference to the phase boundary lines, the majority of the austenite start temperature (A_s) and the austenite finish temperature (A_f) fit within the mixed phase region, reported to be a B33→B2 ($\delta_2 \rightarrow \delta_1$) transformation path. However, the forward transformation on cooling, corresponding to the martensite start temperature (M_s) and the martensite finish temperature (M_f), is not captured within that band. This could be attributed to the construction of a pseudo-binary phase diagram that may not have accounted for the cooling path, or the phenomenon is potentially due to some differences in alloy compositions between this work and others. Nonetheless, it is of importance to note is that the transformation path follows the apparent reported transition from the B33 (Cmcm space group) CrB-type martensite phase to the B2 ($Pm\bar{3}m$ space group) CsCl-type austenite phase.

At high Hf levels, the thermal hysteresis is shown to narrow with added Hf, with a maximum of 201 °C and a minimum of 42 °C for the 40Hf and 50Hf alloys, respectively. However, the trend is not utterly monotonic. In further considering the Yeremenko et al. pseudo-binary phase diagram, the gap reduction between the phase boundaries with the additional Hf (shaded area of Fig. 3) aligns well with the narrowing trend of the hysteresis in these alloys (Table 2).

A representation of the alloys compositional space is shown on the Gibb's triangle of Fig. 4a. The diagram includes data from existing NiTiHf literature obtained from the NASA shape

memory materials analysis and research tool (SM^2ART) database [45, 46], along with data from this recent work. The color map represents the A_s temperature for various alloys. After surveying prior work, it is clear that the compositional space of Hf over 30 at.% has not been explored in the context of shape memory behavior. A new range of transformation temperatures can be obtained surpassing 1000 °C for the A_s. Fig. 4b captures the trend in A_f temperature with Hf addition. For a constant Hf content, a wide range of transformation temperatures can be obtained by varying the Ni content or processing methods – such as hot/cold working or aging heat treatment in the case of slightly Ni-rich formulations. For a constant Ni content, the addition of Hf above 10 at.% results in higher transformation temperatures, and often showed a near linear relationship with temperature. The addition of Hf above 30 at.% also exhibited a near linear trend with an A_f temperature exceeding 1100 °C.

These trends were also established using the modeling framework presented below. Prior work using a similar framework could only be applied to study simple binaries, while this current theoretical and computational developments extended its application to these ternary compositions to quantitatively predict the martensitic transition temperature (MTT), defined as the temperature at which the martensite and the austenite phases have the same value of the Gibbs free energy. Figure 5 compared the calculated MTT with the measured $(M_s + A_f)/2$. Excellent agreement was achieved, and the maximum difference between theory and experiment is 60 K, while the mean absolute error is merely 20 K. The present calculations suggest that vibrational entropy and strong anharmonicity play a central role in the martensitic transitions in the NiTiHf ternaries. In addition, the presented first-principles approach benchmarked by current experiments can be applied to study numerous multi-component highly disordered SMAs.

4.2 Microstructure

Representative SEM micrographs are shown in Fig. 6 corresponding to each alloy composition. Generally, small fractions of HfO_2 inclusions (white particles) are present in all micrographs, in addition to $(Ti,Hf)_4Ni_2O_x$ inclusions (black particles) shown in most alloys, except for the 50Hf composition where the black particles were $Hf_4Ni_2O_x$ type oxides (Fig. 6e). Martensite twins are also visible at this microscale as indicated by the illustrative arrows in Fig. 6c. Some irregularities were observed at the 45Hf content, where a second phase was observed as shown in Fig. 6d. Energy Dispersive X-ray spectroscopy (EDX) indicated that this phase had much higher Hf/Ti ratio as compared to the matrix, even though a homogeneous solid solution was expected based on binary Ni–Ti, Hf–Ti, and Ni–Hf phase diagrams. It is unclear how this second phase forms, keeping in mind that the material was remelted 5 times, then homogenized at 1050 °C. The same alloy was produced several times, with the same second phase forming. Liu et al. [30] also reported a similar microstructure where a secondary phase was observed and attributed to an unknown "τ" phase in the compositional range near the 45Hf content. This unknown phase was neither matched to the Hf_7Ni_{10} phase nor to the Hf_9Ni_{11} phase typically found in 50Hf alloys. This phase was not observed in any of the lower (30-40) Hf alloys (Fig. 6 (a-c)), or in the higher 50Hf alloy (Fig. 6e), and is not shown in the recently reported diagrams by Li and Zheng [47]. However, the presence of micro cracks in select regions of 50Hf were observed as shown in the inset in Fig. 6e.

While SEM provided some general microstructural features, TEM was used to further illustrate the matrix structure in two alloys - the 30Hf and 40Hf compositions. The representative microstructures shown in Fig. 7a and 7d depict a martensitic matrix with a typical plate-like martensite structure containing micro twins. It is frequently reported that the 20Hf composition

consists of a monoclinic (B19') structure, whereas the 50Hf alloys are orthorhombic (B33). In between these two bounds, other phases have been reported as outlined in Table 1, hence the choice of the 30Hf and 40Hf alloys for this TEM work. Using these compositions, selected area diffraction patterns (SADPs) were measured from different areas. In the 30Hf alloys, the majority of the areas within the examined foil were indexed to an orthorhombic B33 phase as shown in Fig. 7b. However, a few SADPs within this alloy composition were uniquely indexed to a monoclinic phase, corresponding to the B19' as shown in Fig. 7c. In the 40Hf alloy, no direct evidence of the B19' phase was found within the inspected foil. These findings help elucidate the presence of both B33 and B19' phases in the 30Hf alloy, but no conclusive evidence of B19' was found in the 40Hf counterpart via TEM.

Additional investigations were conducted on the 30, 35, 40, 45, and 50Hf alloys by collecting crystallographic phase data using the Electron Back Scattered Diffraction (EBSD) technique using SEM. In this method, the lattice interaction with the electron beam at each point creates a pattern of Kikuchi lines that can be indexed for a given phase. The data collected with EBSD are spatially distributed and can be visualized in maps and images, enabling detailed examination of localized features in heterogeneous samples. The phase maps for the two extreme Hf alloys, 30Hf and 50Hf, are shown in Fig. 8(b) and (d), respectively. The band contrast images providing good grain boundary and martensite images of the area scanned are shown in Fig. 8(a) and (c), respectively. In the 30Hf alloy, four phases were detected (Fig. 8b) with majority being the B33 phase, a low fraction of the B19' phase (using the index from previous NiTi-20Hf alloy), and some HfO_2 and $Ti_4Ni_2O_x$ inclusions that were inherently present in the alloy. In the 50Hf alloy, the same phases were present, with the distinction of much less B19' phase fraction. Qualitatively, a phase fraction of under 3 % B19' was present in the 50Hf alloy, compared to

approximately 10% in the 30Hf alloy. Considering the non-equiaxed and large grain size for the cast and homogenized material, these phase fractions did change depending on the area scanned, but B19' was always below 10% with the trend towards decreasing B19' as the Hf content was increased.

For a more quantitative measure of phase fractions, XRD spectra were collected at room temperature for each alloy. A representative spectrum for 50Hf collected with a 2D detector is shown in Fig. 9a. The XRD diffraction patterns collected with a 2D detector consists of concentric spotty rings, where the spots correspond to *hkl* reflection of a crystal with (hkl) planes oriented in the Bragg diffraction conditions. In this material, the spottiness of the diffraction ring is attributed to the crystallites' size given the material was not hot or cold worked to refine the grain structure. For comparison purposes, a diffraction pattern from a 20Hf alloy was also measured as shown in Fig. 9b, where the rings were smooth and corresponded to a 100% B19'structure. The majority of the rings in the 50Hf (Fig. 9a) correspond to the B33 phase shown by the (hkl) indices. However, there remain some small unique reflections from the B19' phase, indicated by the spots in the region between the dotted lines. Commensurate with the microstructural observations from TEM (Fig. 7) and EBSD (Fig. 8), 2D diffraction analyses also indicate that the majority of the phase in 30-50Hf alloys is B33 with a minor amount of B19' that is present in some propensity in all compositions.

Integration of 2D diffraction patterns was performed to obtain the 1D intensity as a function of 2θ pattern, as shown in Fig. 10. Rietveld refinement was performed to quantify the phase identification for each sample as shown for the representative 50Hf alloy. As expected, most reflections fit the B33 phase, with only a few small peaks fitting to the B19' phase. It is also evident that this refinement did not capture some peaks corresponding to other phases, resulting

in a suboptimal fit. Other phases such as the orthorhombic B19, Ti_2Ni, Hf_7Ni_{10} and the Hf_9Ni_{11} were tried in the refinement but did not uniquely fit the profile. Oxides such as HfO_2 and $NiHfO_x$ were also fit to this pattern but did not match the peaks under investigation. Regardless of the suboptimal fits, the B19' and B33 phases were confirmed in each alloy.

A summary of XRD patterns corresponding to every alloy is shown in Fig. 11. For clarity, diffraction patterns were offset and separated into sub-groups in order to better visualize the peak evolution with the added Hf. A 20Hf alloy diffraction pattern with 100% B19' phase is also included as a reference. It is observed that starting from the 30Hf alloy and above, the material mostly fits a B33 pattern, with a small volume fraction of B19' and oxide phases, in agreement with EBSD and TEM findings. Figure 11a illustrates the $(021)_{B33}$ and $(110)_{B33}$ orthorhombic B33 peak evolution with the addition of Hf. These shifts also correspond to lattice parameter changes as reported in Table 3. Figure 11b is an example case where the $(002)_{B19'}$ and $(\bar{1}11)_{B19'}$ reflections are also present in a small fraction even in the 50Hf alloy. It is interesting to note how certain B19' reflections existing in the 20Hf diminish and disappear as a function of additional Hf content (Fig. 11c-e). This is very apparent in Fig. 11c with the $(012)_{B19'}$ reflections diminishing at the expense of $(002)_{B33}$ and other B33 reflections.

As seen throughout these microstructural results (TEM, EBSD and XRD), clearly the major stable phase in 30-50Hf alloys at room temperature is the B33 phase that transforms to the B2 phase at higher temperature as outlined in the thermal analysis section. It is also established using the modeling framework that the transformation path from a B19' to a B2 exists at Hf content at or below 20 at.%, whereas for higher Hf content the transition preferentially follows the B33 to B2 path, based on free energy calculations and comparison of the B19' and B33 phases.

4.3 Thermomechanical Response

Observations of reversible phase change as mainly evident by the DSC thermographs do not guarantee that the alloys can exhibit a shape change (shape recovery) at the macroscopic level. In fact, it is arguable whether this solid-to-solid, diffusionless phase transformation is considered a martensitic transformation given the B33 is not a crystallographic subgroup of the B2 phase. As a starting point, a set of UPFR tests were performed to evaluate the stress-strain behavior and the shape memory effect. Fig. 12 is a set of compressive stress-strain responses (Fig. 12a-e), where the material was tested up to 1 GPa followed by unloading to zero stress. In comparing the different alloys, the strain at maximum stress increased with the addition of Hf, ranging from 1.7% to 7% in the 30Hf and 50Hf alloys, respectively. Specimens were then subjected to multiple thermal cycles between room temperature and up to 1300 °C under no applied stress in a dilatometer, as shown in Fig. 12a'-e'. Recovery strains were at 100% in the 30Hf alloys and gradually diminished to nearly 0% in the 50Hf alloy. A summary of the pointwise data corresponding to the measured values of maximum loading strain, unloaded strain and the recovery strain is shown in Fig. 13. It can be noted that with increasing Hf content, the apparent yield stress of the material decreases, contributing to a higher maximum loading strain at 1 GPa (Fig. 13a), and more of this strain being retained after unloading (Fig. 13b). Given the high transformation temperatures in this alloy, the thermal expansion plays a significant role, and can even exceed the recoverable strains due to the martensitic transformation. Additionally, with the added Hf giving rise to higher transformation temperatures, plasticity mechanisms also become dominant and compete with the martensitic transformation, leading to a lower percentage of recovery of the unloaded strain for the higher Hf alloys (Fig. 13c).

The conjugate experiment frequently used for evaluating shape memory behavior, particularity work output potential, use the UCFTC test method. This was applied to the 30Hf and 35Hf alloys as shown in Fig. 14. For the 30Hf alloy (Fig. 14a) typical hysteresis loops are obtained while cycling under a constant compressive stress from 50 to 200 MPa. The magnitude of work output is on the order of 3.58 J/cm^3 with a recoverable strain of 1.79% on heating under the 200 MPa stress. Simultaneously with phase transformation, the material deforms by creep/plasticity in the austenitic phase, leading to very large irrecoverable strains. This behavior is known to be active in NiTi-based alloys operated at elevated temperature such as in NiTi [48], NiTiPd [49], and NiTiHf [50] alloys. At 300 MPa, creep processes at temperatures above 700ºC become dominant, as evident in the downward curve (increasing strain) in the heating curve above 700 ºC, but the material still possesses a very respectable one-way transformation strain during heating of 2.72% equivalent to 8.16 J/cm^3 in work output. A more pronounced creep effect is shown in Fig. 14b (corresponding to the 35Hf alloy) during heating, where transformation strains are overwhelmed by creep strains, rendering an unserviceable work output during the heating segment. The rest of the alloys were not tested using this methodology due to the expected substandard shape memory behavior, and the high temperatures required to cycle through the transformation under stress.

5. Concluding Remarks

A set of vacuum arc melted NiTiHf shape memory alloys with 30 to 50 at.% Hf were investigated. Phase identification along with shape memory behavior were evaluated using microstructural evaluations (SEM, TEM, EBSD and XRD), and thermomechanical experiments (DSC, dilatometry, UPFF and UCFTC). The following conclusions can be made:

- The low temperature phase in the 30 to 50 at.% Hf content is composed primarily of an orthorhombic B33 (Cmcm space group) CrB-type martensite phase with small traces of the monoclinic B19' ($P112_1/m$ space group) martensite phase. On continued heating, all phases transform to the B2 ($Pm\bar{3}m$ space group) CsCl-type austenite phase.
- SEM and EBSD micrographs show presence of intermetallic inclusions of the type HfO_2, $Ti_4Ni_2O_x$ and $HfNiO_x$ oxides. Matrix phase identification at room temperature where the low temperature phase exists was done using EBSD and TEM.
- XRD measurements were performed in 1D and 2D modes to reveal the phase fractions of the low temperature phase. XRD spectra confirmed the major matrix phase to be B33 and detected the presence of a small amount of B19' phase in all compositions. The 2D scans showed clearer results and confirmed a small volume fraction of B19' in all compositions.
- UPFR experiments up to 1 GPa compressive stress showed strain recovery of nearly 100% in the 30Hf alloy that diminishes with Hf addition to nearly 0% in the 50Hf alloy due to the activation of plastic mechanisms. Thermal strains play a significant role in these high temperature alloys, often competing with transformation strains, in addition to unrecovered strains due to plasticity.
- UCFTC experiments revealed limited work output at high temperatures, with a work output of approximately 8.16 J/cm^3 in compression. Transformation strains were hindered by creep-dominant mechanisms simultaneously occurring during the phase transformation process and at higher temperatures in the austenite.
- First-principles calculations accurately predict the phase transitions and the transition temperatures in complicated ternary SMAs, demonstrating the central role played by the

vibrational entropy and strong anharmonicity as revealed through extended computational capability.

In this initial work, the alloys were examined without the compounded effects of hot or cold working, precipitation strengthening, or other stabilizing factors, to assess feasibility of these alloys as potential high temperature material. Future work will focus on strengthening mechanisms to enhance the shape memory effect at elevated temperatures.

6. Acknowledgments

Funding from the NASA Aeronautics Research Mission Directorate (ARMD) Transformational Tools and Technologies (TTT) project is gratefully acknowledged.

References

[1] O. Benafan, G.S. Bigelow, A. Garg, R.D. Noebe, D.J. Gaydosh, R.B. Rogers, Processing and scalability of NiTiHf high-temperature shape memory alloys, Shape Memory and Superelasticity 7(1) (2021) 109-165.
[2] Y. Yamabe-Mitarai, TiPd-and TiPt-Based High-Temperature Shape Memory Alloys: A Review on Recent Advances, Metals 10(11) (2020) 1531.
[3] K. Chastaing, A. Denquin, R. Portier, P. Vermaut, High-temperature shape memory alloys based on the RuNb system, Materials Science and Engineering: A 481 (2008) 702-706.
[4] D. Canadinc, W. Trehern, J. Ma, I. Karaman, F. Sun, Z. Chaudhry, Ultra-high temperature multi-component shape memory alloys, Scripta Materialia 158 (2019) 83-87.
[5] D.N. AbuJudom II, P.E. Thoma, M.-Y. Kao, D.R. Angst, High transformation temperature shape memory alloy, U.S. Patent No. 5,114,504, 1992.
[6] D.R. Angst, P.E. Thoma, M.Y. Kao, The Effect of Hafnium Content on the Transformation Temperatures of Ni49Ti51-xHfx. Shape Memory Alloys, J. Phys. IV France 05(C8) (1995) C8-747-C8-752.
[7] Z.J. Pu, H.-K. Tseng, K.-H. Wu, Innovative system of high-temperature shape memory alloys, Proc. SPIE 2189, Smart Structures and Materials 1994: Smart Materials, 1994, pp. 289-297.
[8] Y. Zhu, Z. Pu, C. Li, K. Wu, Stability of NiTi-Pd and NiTi-Hf high temperature shape memory alloys, Florida International Univ., Miami, FL (United States), 1994.
[9] K.-H. Wu, Z.J. Pu, H.-K. Tseng, F.S. Biancaniello, The Shape Memory Effect of the NiTi-Hf High Temperature Shape Memory Alloy, Proc. The 1st International Conference on Shape Memory and Superelastic Technologies, Pacific Grove, CA, 1994, pp. 61-66.
[10] P.L. Potapov, A.V. Shelyakov, A.A. Gulyaev, E.L. Svistunov, N.M. Matveeva, D. Hodgson, Effect of Hf on the structure of Ni-Ti martensitic alloys, Materials Letters 32(4) (1997) 247-250.

[11] H. Gu, K. Leung, C. Chung, Growth of high-temperature NiTi 1− x Hf x shape memory alloy thin films by laser ablation of composite targets, Journal of Vacuum Science & Technology A: Vacuum, Surfaces, and Films 16(6) (1998) 3420-3422.
[12] S.-H. Kang, T.-H. Nam, Crystal structure of (TiHf) Ni phase formed in a 20Ti− 50Ni− 30Hf (at.%) alloy, Metals and Materials International 7(5) (2001) 443-446.
[13] S. Sanjabi, Y. Cao, Z. Barber, Multi-target sputter deposition of Ni50Ti50− xHfx shape memory thin films for high temperature microactuator application, Sensors and Actuators A: Physical 121(2) (2005) 543-548.
[14] A.J. Muir Wood, S. Sanjabi, Y.Q. Fu, Z.H. Barber, T.W. Clyne, Nanoindentation of binary and ternary Ni–Ti-based shape memory alloy thin films, Surface and Coatings Technology 202(13) (2008) 3115-3120.
[15] Y. Tong, Y. Liu, J. Miao, Phase transformation in NiTiHf shape memory alloy thin films, Thin Solid Films 516(16) (2008) 5393-5396.
[16] J. Rao, T. Roberts, K. Lawson, J. Nicholls, Nickel titanium and nickel titanium hafnium shape memory alloy thin films, Surface and Coatings Technology 204(15) (2010) 2331-2336.
[17] R. Santamarta, R. Arróyave, J. Pons, A. Evirgen, I. Karaman, H. Karaca, R. Noebe, TEM study of structural and microstructural characteristics of a precipitate phase in Ni-rich Ni–Ti–Hf and Ni–Ti–Zr shape memory alloys, Acta Materialia 61(16) (2013) 6191-6206.
[18] L. Patriarca, H. Sehitoglu, High-temperature superelasticity of $Ni_{50.6}Ti_{24.4}Hf_{25.0}$ shape memory alloy, Scripta Materialia 101 (2015) 12-15.
[19] L. Patriarca, H. Sehitoglu, E.Y. Panchenko, Y. Chumlyakov, High-temperature functional behavior of single crystal $Ni_{51.2}Ti_{23.4}Hf_{25.4}$ shape memory alloy, Acta Materialia 106 (2016) 333-343.
[20] W. Abuzaid, H. Sehitoglu, Functional fatigue of $Ni_{50.3}Ti_{25}Hf_{24.7}$–Heterogeneities and evolution of local transformation strains, Materials Science and Engineering: A 696 (2017) 482-492.
[21] H. Sehitoglu, Y. Wu, L. Patriarca, Shape memory functionality under multi-cycles in NiTiHf, Scripta Materialia 129 (2017) 11-15.
[22] A.N. Bucsek, G.A. Hudish, G.S. Bigelow, R.D. Noebe, A.P. Stebner, Composition, compatibility, and the functional performances of ternary NiTiX high-temperature shape memory alloys, Shape Memory and Superelasticity 2(1) (2016) 62-79.
[23] T. Umale, D. Salas, B. Tomes, R. Arroyave, I. Karaman, The effects of wide range of compositional changes on the martensitic transformation characteristics of NiTiHf shape memory alloys, Scripta Materialia 161 (2019) 78-83.
[24] V. Yeremenko, E. Semenova, L. Tretyachenko, V. Petyukh, Constitution of the Hf-Ni system up to 50 at.% Ni, Journal of alloys and compounds 191(1) (1993) 117-119.
[25] K. Gupta, The Hf-Ni-Ti (hafnium-nickel-titanium) system, Journal of phase equilibria 22(1) (2001) 69-72.
[26] G. Cacciamani, P. Riani, F. Valenza, Equilibrium between MB2 (M= Ti, Zr, Hf) UHTC and Ni: a thermodynamic database for the B–Hf–Ni–Ti–Zr system, Calphad 35(4) (2011) 601-619.
[27] P. Nash, A. Nash, The Hf-Ni (hafnium-nickel) system, Bulletin of Alloy Phase Diagrams 4(3) (1983) 250-253.
[28] E.L. Semenova, The Solidus Surface in the Ti—Ni—Hf System in the Ti—TiNi—HfNi—Hf Region, Powder Metallurgy and Metal Ceramics 40(7) (2001) 414-425.

[29] A.J. Ross, T. Gheno, P.K. Ray, M.J. Kramer, X.L. Liu, G. Lindwall, B. Zhou, S.L. Shang, B. Gleeson, Z.K. Liu, A first-principles based description of the Hf-Ni system supported by high-temperature synchrotron experiments, Thermochimica Acta 668 (2018) 142-151.
[30] J. Liu, L. Zhu, X. Huang, G. Cai, Z. Jin, Investigation of the phase equilibria in Ti-Ni-Hf system using diffusion triples and equilibrated alloys, Calphad 58 (2017) 160-168.
[31] ASTM E3097-17, Standard Test Method for Mechanical Uniaxial Constant Force Thermal Cycling of Shape Memory Alloys, ASTM International, West Conshohocken, PA, 2017, www.astm.org.
[32] ASTM E3098-17, Standard Test Method for Mechanical Uniaxial Pre-strain and Thermal Free Recovery of Shape Memory Alloys, ASTM International, West Conshohocken, PA, 2017, www.astm.org.
[33] A. Zunger, S.-H. Wei, L. Ferreira, J.E. Bernard, Special quasirandom structures, Physical review letters 65(3) (1990) 353.
[34] A. Van de Walle, P. Tiwary, M. De Jong, D. Olmsted, M. Asta, A. Dick, D. Shin, Y. Wang, L.-Q. Chen, Z.-K. Liu, Efficient stochastic generation of special quasirandom structures, Calphad 42 (2013) 13-18.
[35] G. Kresse, J. Hafner, Ab initio molecular dynamics for liquid metals, Physical review B 47(1) (1993) 558.
[36] G. Kresse, J. Hafner, Ab initio molecular-dynamics simulation of the liquid-metal–amorphous-semiconductor transition in germanium, Physical Review B 49(20) (1994) 14251.
[37] G. Kresse, J. Furthmüller, Efficiency of ab-initio total energy calculations for metals and semiconductors using a plane-wave basis set, Computational materials science 6(1) (1996) 15-50.
[38] G. Kresse, J. Furthmüller, Efficient iterative schemes for ab initio total-energy calculations using a plane-wave basis set, Physical review B 54(16) (1996) 11169.
[39] J.P. Perdew, K. Burke, M. Ernzerhof, Generalized gradient approximation made simple, Physical review letters 77(18) (1996) 3865.
[40] P.E. Blöchl, Projector augmented-wave method, Physical review B 50(24) (1994) 17953.
[41] G. Kresse, D. Joubert, From ultrasoft pseudopotentials to the projector augmented-wave method, Physical review b 59(3) (1999) 1758.
[42] Z. Wu, J.W. Lawson, Theoretical investigation of phase transitions in the shape memory alloy NiTi, Physical Review B 106(14) (2022) L140102.
[43] ASTM F2004-17, Standard Test Method for Transformation Temperature of Nickel-Titanium Alloys by Thermal Analysis, ASTM International, West Conshohocken, PA, 2017, www.astm.org, 2017.
[44] G. Wolten, Diffusionless phase transformations in zirconia and hafnia, Journal of the American Ceramic Society 46(9) (1963) 418-422.
[45] O. Benafan, G.S. Bigelow, A.W. Young, Shape Memory Materials Database Tool—A Compendium of Functional Data for Shape Memory Materials, Advanced Engineering Materials 22(7) (2020) 1901370.
[46] P.E. Caltagirone, O. Benafan, Shape Memory Materials Database and Analysis Tool: Finding Data Anomalies & Trends, Shape Memory and Superelasticity (2023).
[47] K. Li, W. Zheng, Thermodynamic modeling of the Ni–Ti–Hf system, Calphad 81 (2023) 102558.

[48] S. Raj, R. Noebe, Low temperature creep of hot-extruded near-stoichiometric NiTi shape memory alloy part II: Effect of thermal cycling, Materials Science and Engineering: A 581 (2013) 154-163.
[49] P.K. Kumar, U. Desai, J.A. Monroe, D.C. Lagoudas, I. Karaman, G. Bigelow, R.D. Noebe, Experimental investigation of simultaneous creep, plasticity and transformation of Ti50. 5Pd30Ni19. 5 high temperature shape memory alloy during cyclic actuation, Materials Science and Engineering: A 530 (2011) 117-127.
[50] P.S. Chaugule, O. Benafan, J.-B. le Graverend, Phase transformation and viscoplasticity coupling in polycrystalline nickel-titanium-hafnium high-temperature shape memory alloys, Acta Materialia 221 (2021) 117381.

Figures

Figure 1: DSC scans corresponding to the 2nd and 5th cycles. Thermographs were vertically stacked for better visualization.

Figure 2: DSC peak evolution as a function of cycles for the NiTi-30Hf alloy during heating. (a) Entire scan showing both matrix phase transformation around 600° C, and HfO_2 oxide phase transformation around 1175°C, and (b) magnified view of the oxide peak evolution with cycling. T_s and T_f are the monoclinic-to-tetragonal transformation start and finish temperatures, respectively, for the HfO_2.

Figure 3: Measured transformation temperatures as a function of Hf content. The shaded area is bordered by the phase boundary lines adopted from Yeremenko et al. [24], with the reported crystal structures type δ_1 (B2 - CsCl-type) and δ_2 (B33 - CrB-type). A_s, A_f M_s and M_f are the austenite start, austenite finish, martensite start, and martensite finish temperatures, respectively.

Figure 4: NiTiHf alloy compositions as a function of transformation temperatures including alloys previously studied and alloys of the current work. (a) Composition space in Gibb's triangle, and (b) austenite finish temperature as function of Hf content. Data from existing NiTiHf literature was obtained from the NASA shape memory materials analysis and research tool (SM^2ART) database [45, 46].

Figure 5: Measured and computed martensitic transformation temperatures as a function of Hf content from 30 to 50 Hf at.%. Ni content is set to 50 at.% throughout.

Figure 6: SEM micrographs of as cast and homogenized (a) 30Hf, (b) 35Hf, (c) 40Hf, (d) 45Hf, (e) 50Hf alloys.

Figure 7: TEM micrographs and selected area diffraction patterns for (a-c) 30Hf alloy, and (d-f) 40Hf alloy.

Figure 8: Band contrast and EBSD crystallographic data for (a-b) 30Hf alloy and (c-d) 50Hf alloy.

Figure 9: Two-dimensional XRD patterns for (a) 50Hf and (b) 20Hf alloys. Area between the dotted lines corresponds to B19' reflections.

Figure 10: Whole 1D XRD pattern Rietveld refinement for the 50Hf alloy. The measured data are indicated by the solid line, and the calculated profile is indicated by the dashed gray line. The tick marks below the profile pattern indicate the reflections from B33 and B19' phases. The lower curve is the difference between the measurement and refinement.

Figure 11: Stacked XRD patterns corresponding to all alloy compositions and sub-sections for better visualization.

Figure 12: Uniaxial pre-strain and free recovery results showing (a-e) the stress-strain behavior during loading to 1 GPa and unloading, and (a'-e') temperature-strain response during heating and cooling.

Figure 13: Uniaxial pre-strain and free recovery pointwise data corresponding to (a) maximum loading strain, (b) unloaded strain, and (c) recovery ratio.

Figure 14: Uniaxial constant force thermal cycling tests for (a) 30Hf and (b) 35Hf alloys subjected to several stress levels.

Figure 1

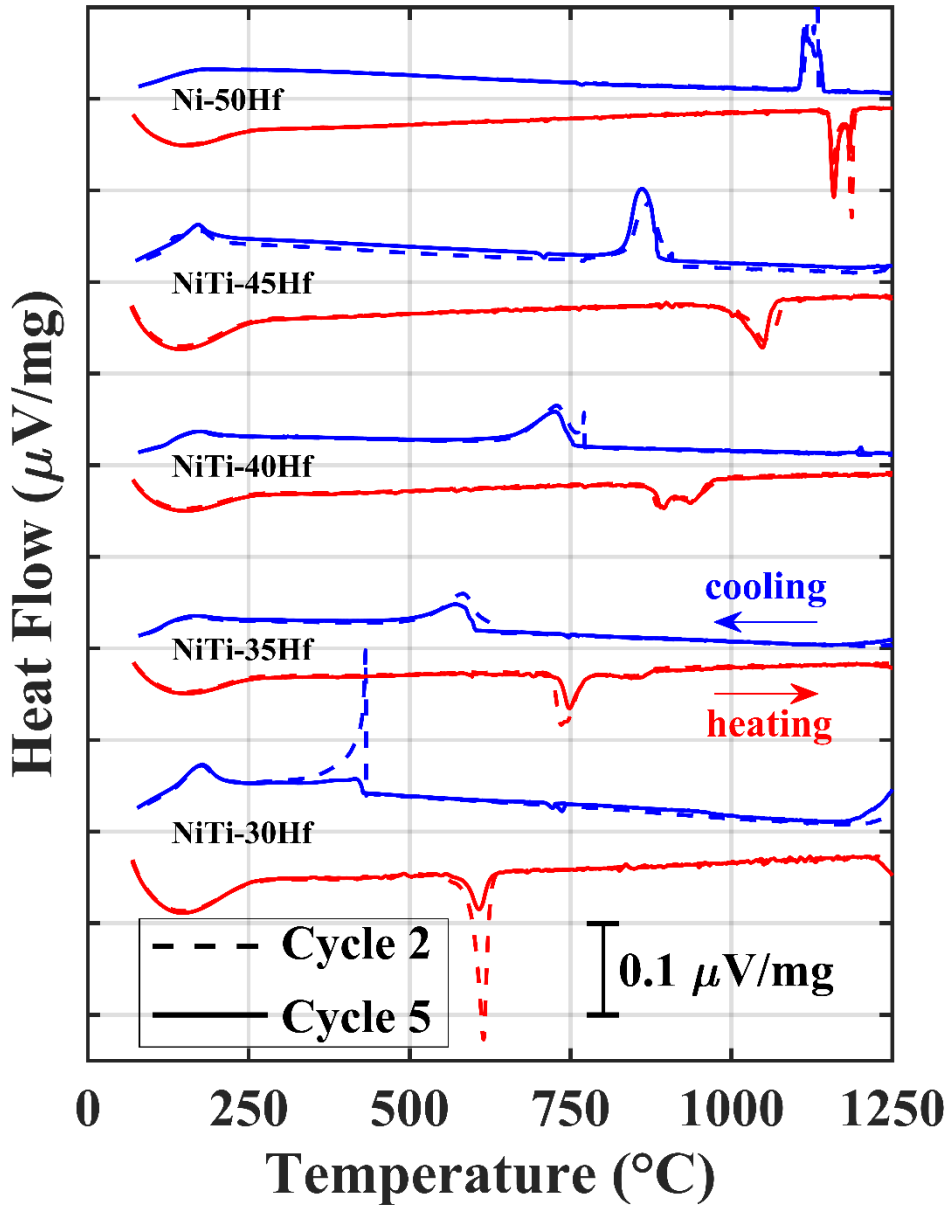
Ni-50Hf
NiTi-45Hf
NiTi-40Hf
NiTi-35Hf
NiTi-30Hf
cooling
heating
Cycle 2
Cycle 5
0.1 μV/mg
Heat Flow (μV/mg)
0
250
500
750
1000
1250
Temperature (°C)

Figure 2

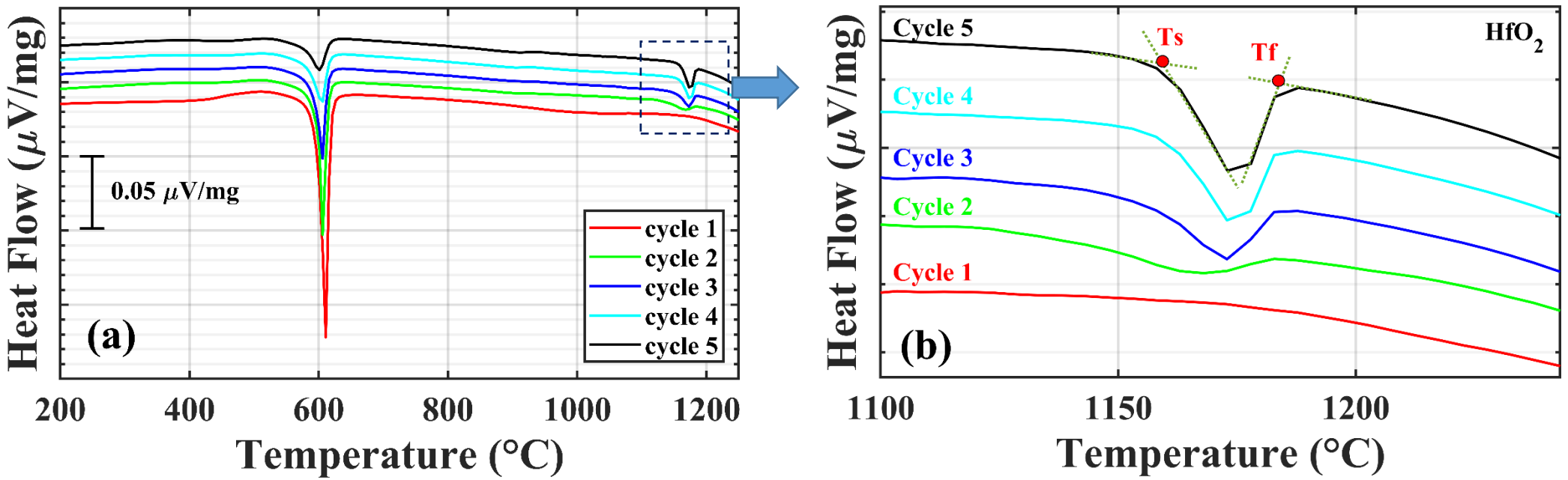
Heat Flow (μV/mg)
0.05 μV/mg
(a)
cycle 1
cycle 2
cycle 3
cycle 4
cycle 5
200
400
600
800
1000
1200
Temperature (°C)
Cycle 5
Ts
Tf
HfO2
Cycle 4
Cycle 3
Cycle 2
Cycle 1
(b)
1100
1150
1200
Temperature (°C)

Figure 3

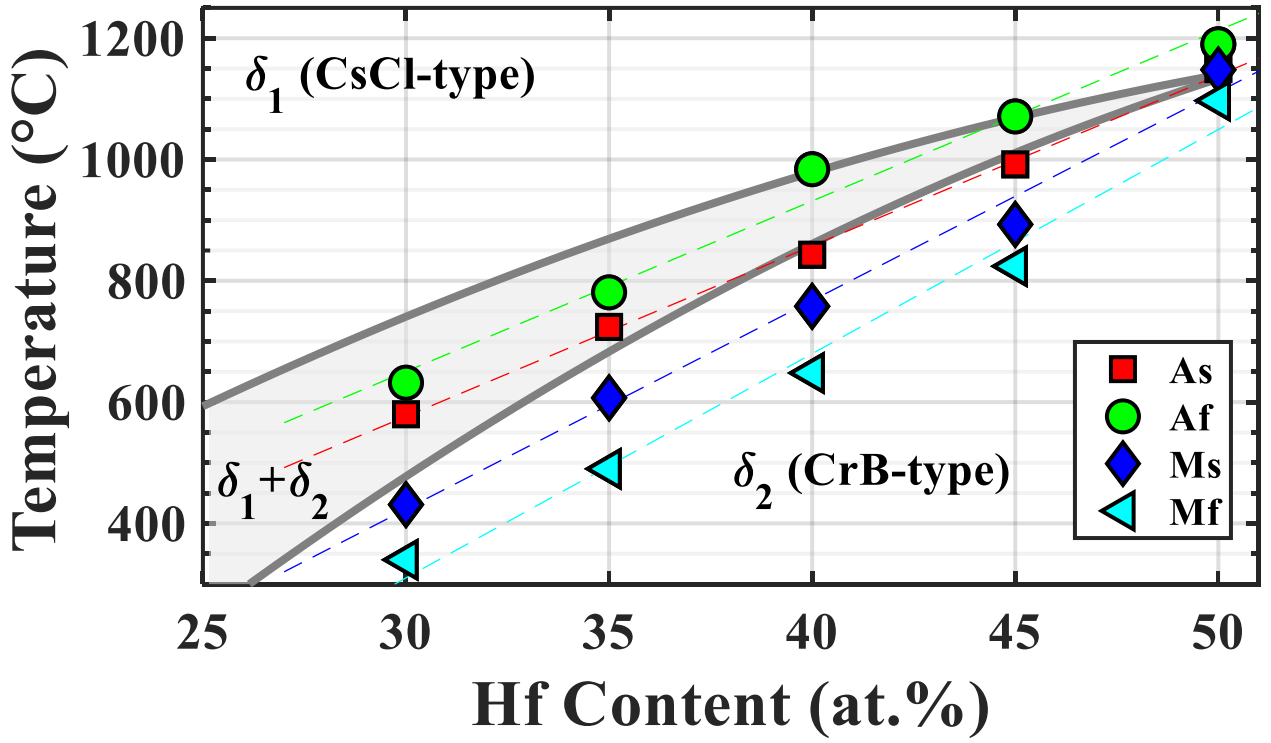
Temperature (°C)
1200
1000
800
600
400
25
30
35
40
45
50
Hf Content (at.%)
δ1 (CsCl-type)
δ1+δ2
δ2 (CrB-type)
As
Af
Ms
Mf

Figure 4

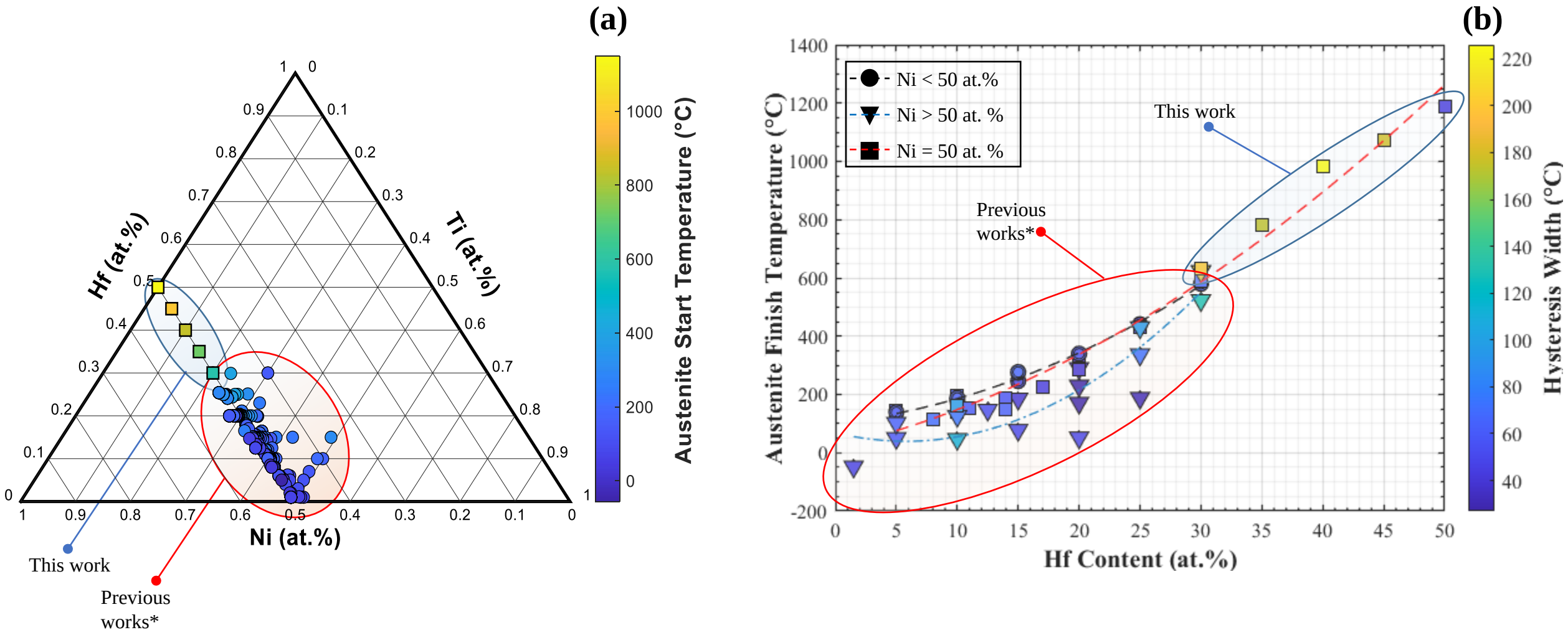
(a)
Hf (at.%)
Ti (at.%)
Ni (at.%)
Austenite Start Temperature (°C)
This work
Previous works*
(b)
Ni < 50 at.%
Ni > 50 at. %
Ni = 50 at. %
This work
Previous works*
Austenite Finish Temperature (°C)
Hf Content (at.%)
Hysteresis Width (°C)

Figure 5

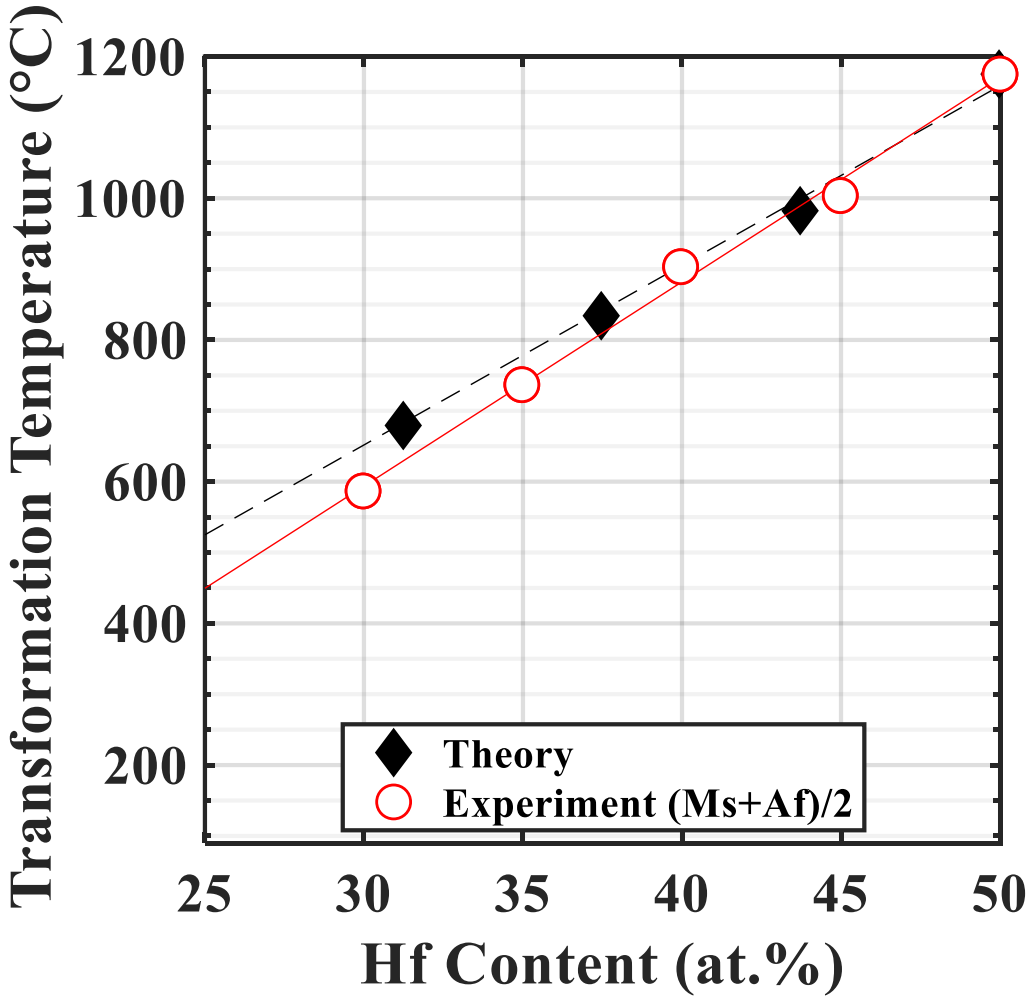
Transformation Temperature (°C)
1200
1000
800
600
400
200
25
30
35
40
45
50
Hf Content (at.%)
Theory
Experiment (Ms+Af)/2

Figure 6

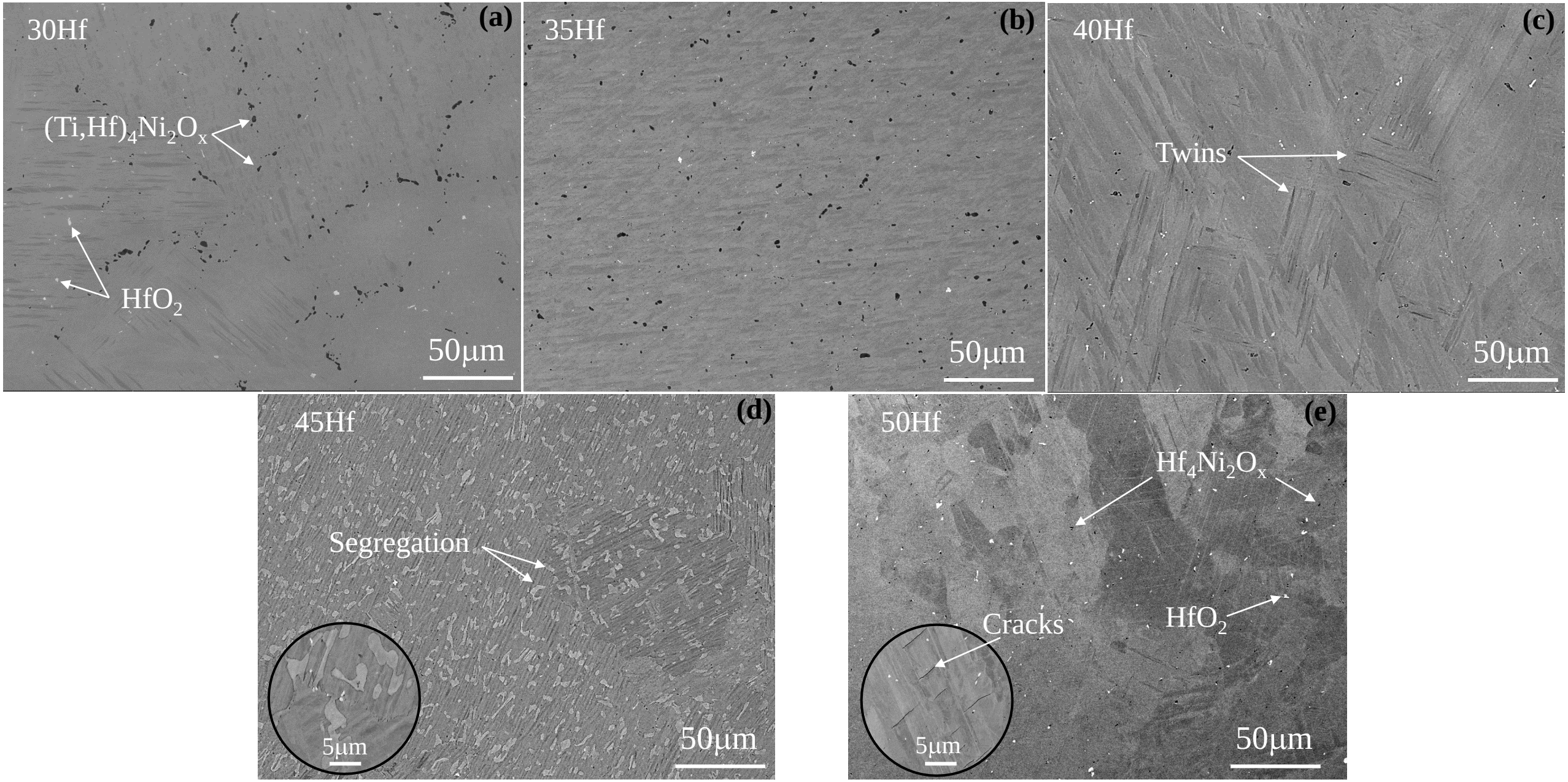
30Hf
(a)
(Ti,Hf)4Ni2Ox
HfO2
50μm
35Hf
(b)
50μm
40Hf
(c)
Twins
50μm
45Hf
(d)
Segregation
5μm
50μm
50Hf
(e)
Hf4Ni2Ox
Cracks
HfO2
5μm
50μm

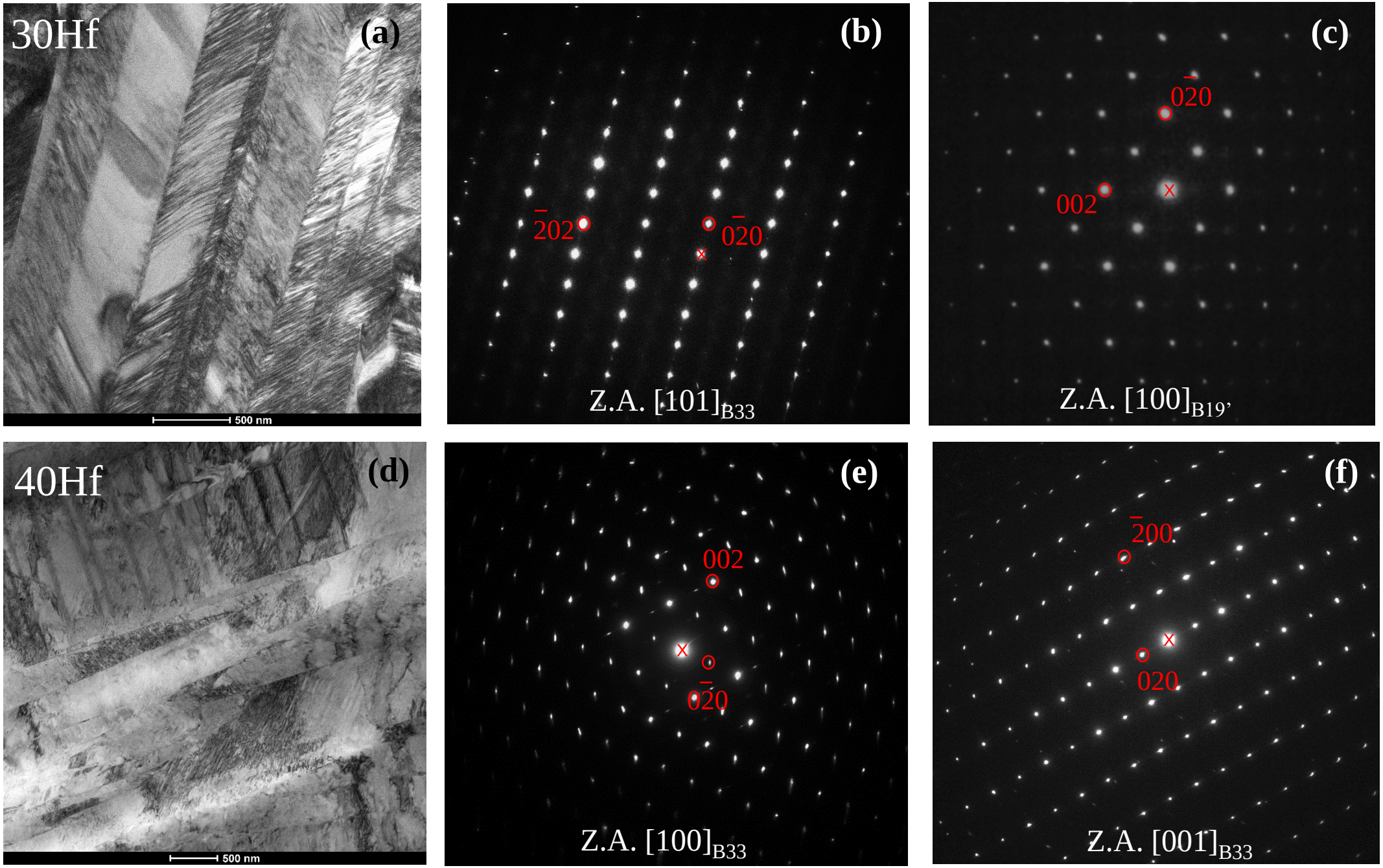
30Hf
(a)
500 nm
(b)
$\bar{2}02$
$0\bar{2}0$
Z.A. $[101]_{B33}$
(c)
$0\bar{2}0$
002
Z.A. $[100]_{B19'}$
40Hf
(d)
500 nm
(e)
002
$0\bar{2}0$
Z.A. $[100]_{B33}$
(f)
$\bar{2}00$
020
Z.A. $[001]_{B33}$

Figure 7

Figure 8

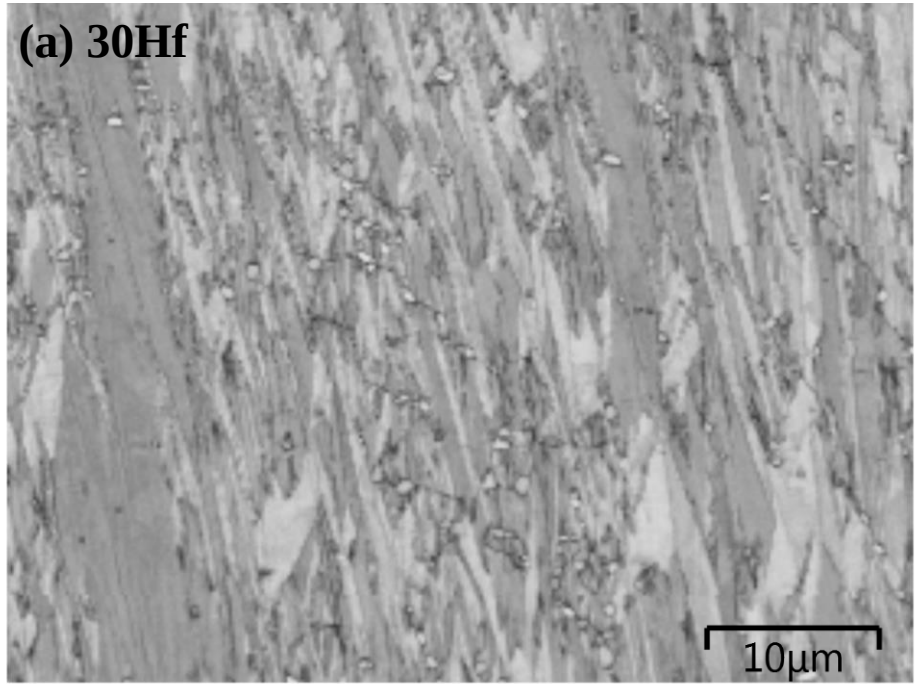
(a) 30Hf
10μm

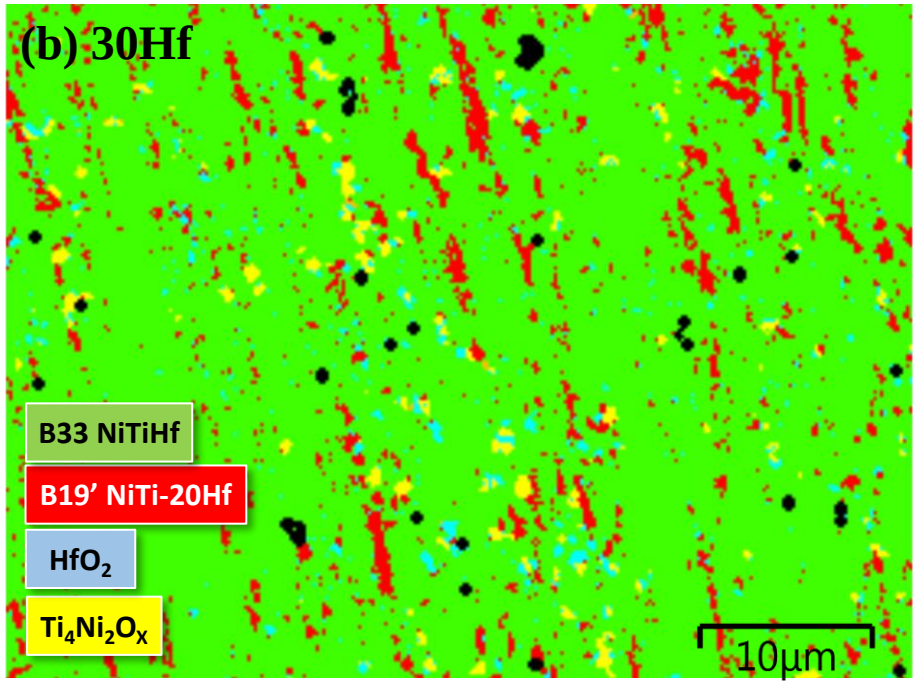
(b) 30Hf
B33 NiTiHf
B19' NiTi-20Hf
HfO2
Ti4Ni2Ox
10μm

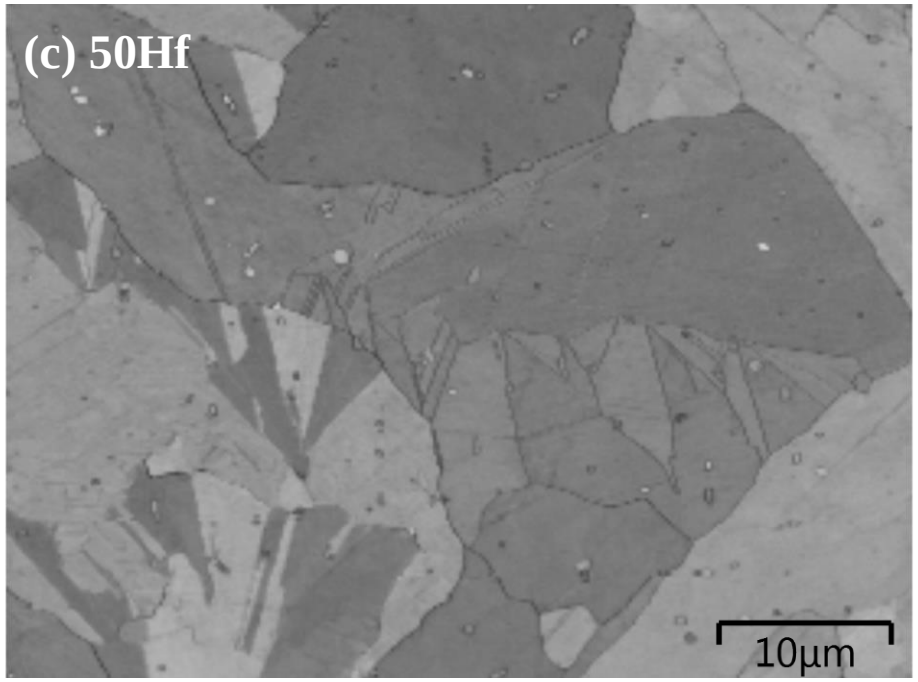
(c) 50Hf
10μm

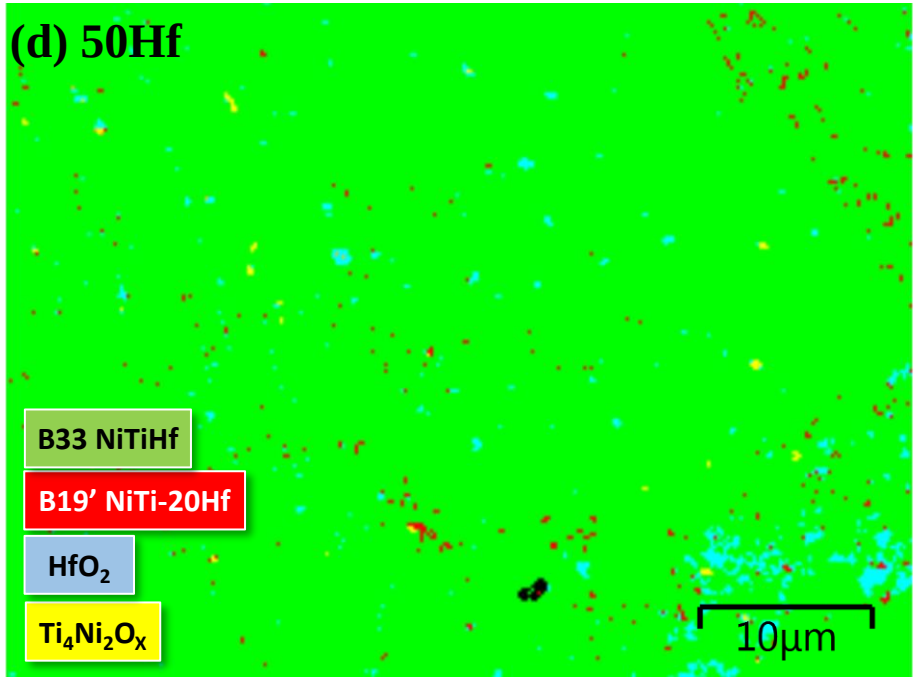
(d) 50Hf
B33 NiTiHf
B19' NiTi-20Hf
HfO2
Ti4Ni2Ox
10μm

Figure 9

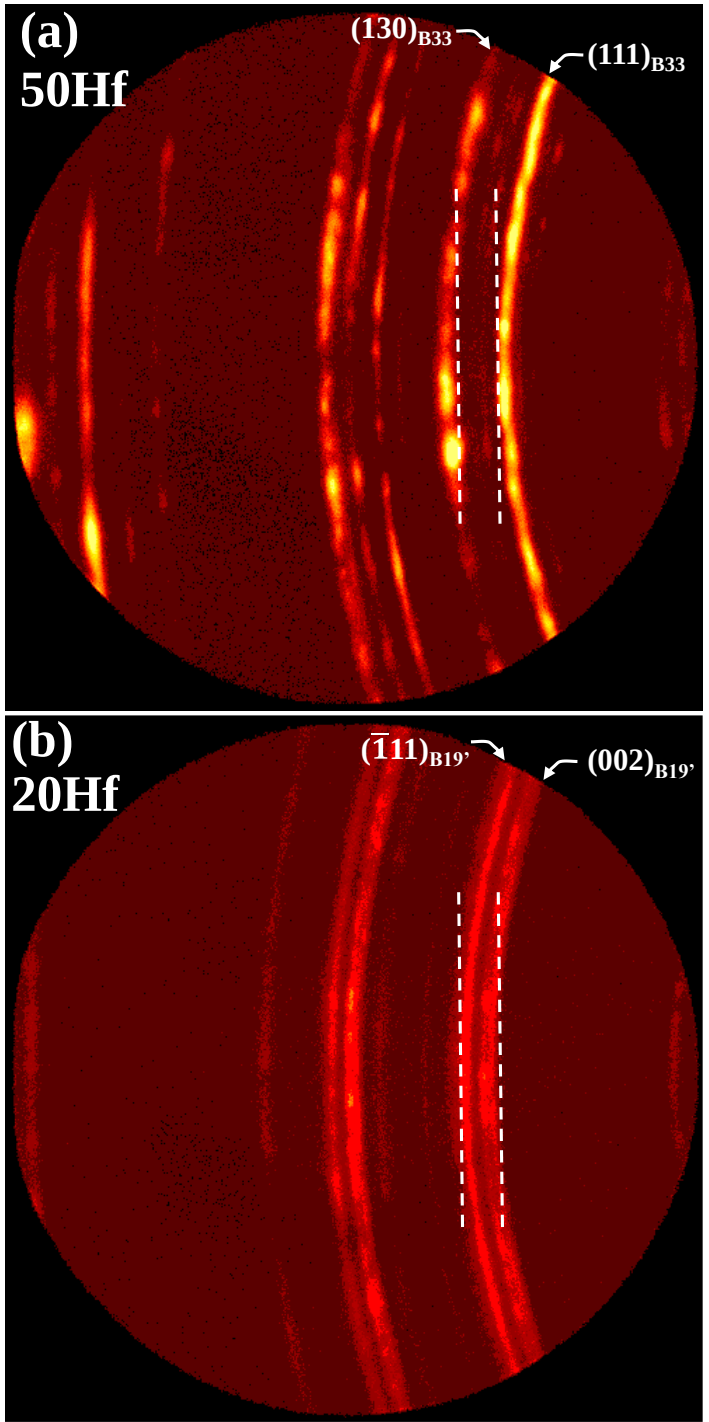

Figure 10

Refinement

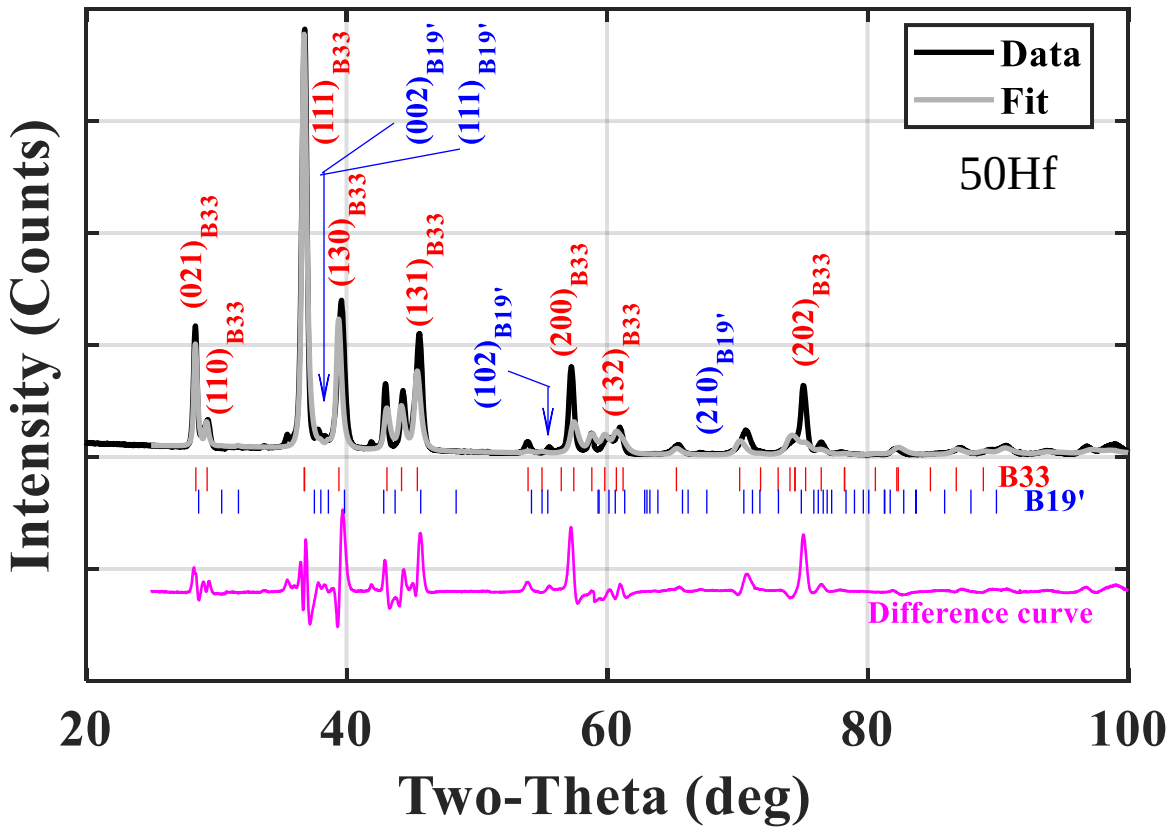

Figure 11

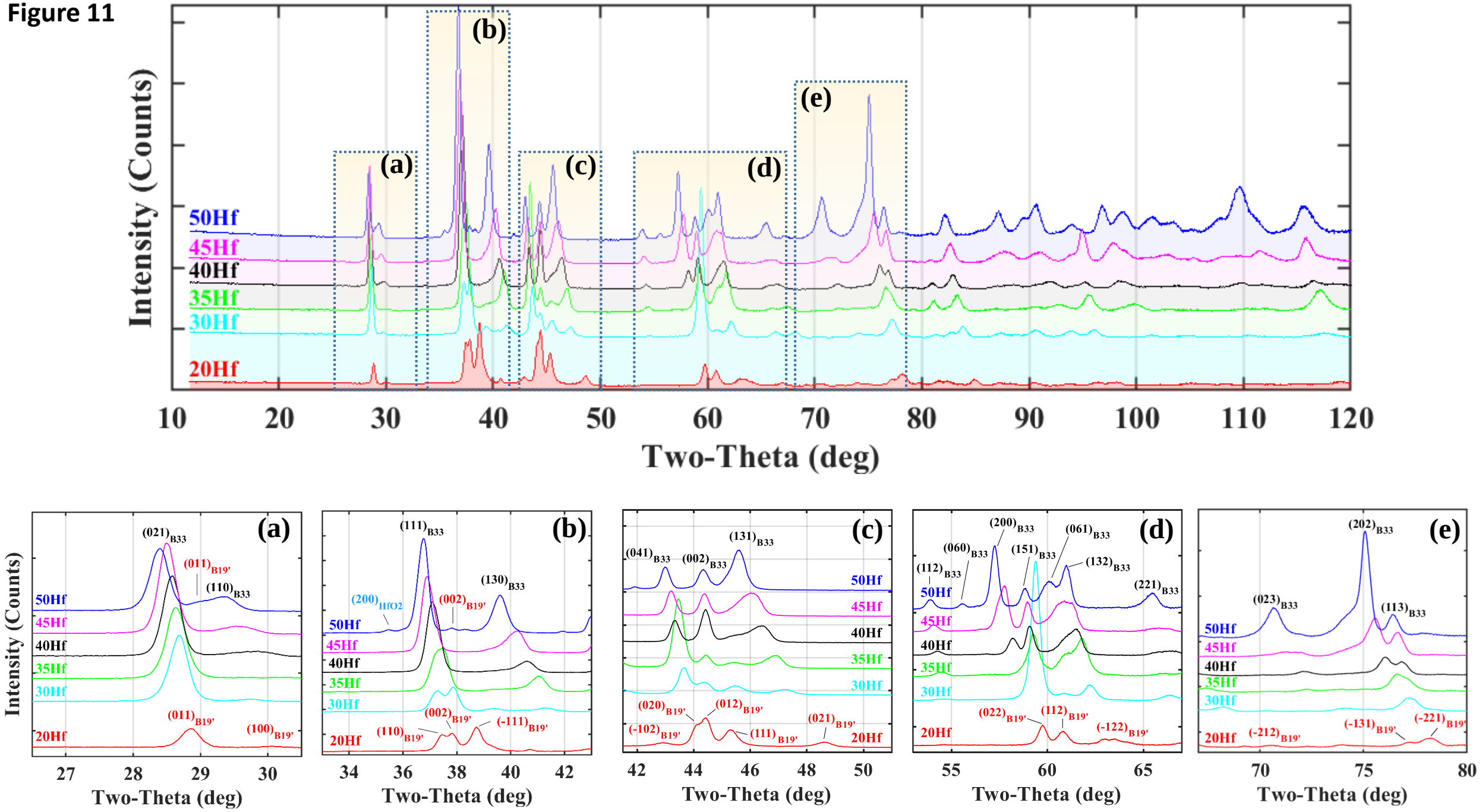
(a)
(b)
(c)
(d)
(e)
50Hf
45Hf
40Hf
35Hf
30Hf
20Hf
Intensity (Counts)
Two-Theta (deg)
(021)B33
(011)B19'
(110)B33
(100)B19'
(111)B33
(200)HfO2
(002)B19'
(130)B33
(110)B19'
(-111)B19'
(041)B33
(002)B33
(131)B33
(020)B19'
(012)B19'
(-102)B19'
(111)B19'
(021)B19'
(112)B33
(060)B33
(200)B33
(151)B33
(061)B33
(132)B33
(221)B33
(022)B19'
(112)B19'
(-122)B19'
(202)B33
(023)B33
(113)B33
(-212)B19'
(-131)B19'
(-221)B19'

Figure 12

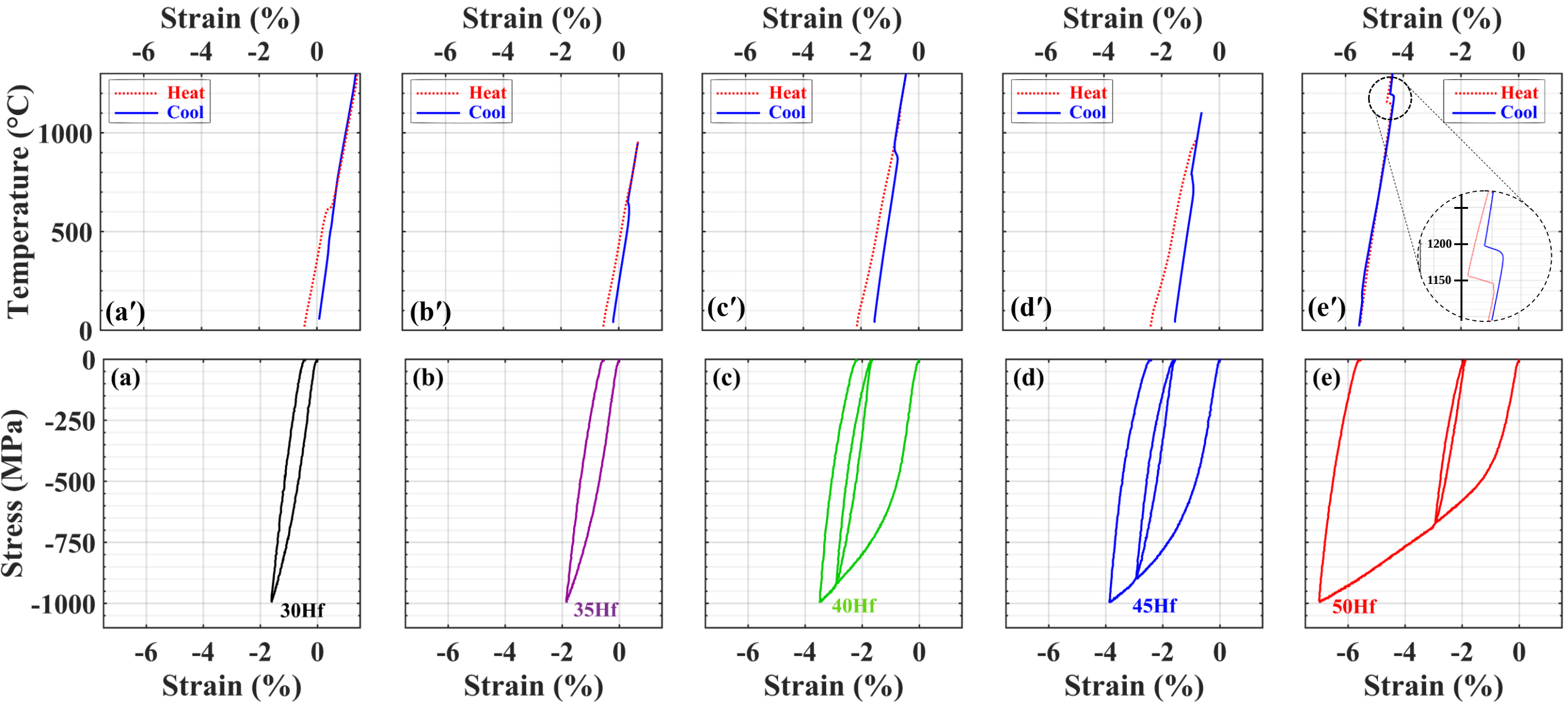
Strain (%)
-6 -4 -2 0
Heat
Cool
Temperature (°C)
1000
500
0
(a′)
(b′)
(c′)
(d′)
(e′)
1200
1150
Stress (MPa)
0
-250
-500
-750
-1000
(a)
(b)
(c)
(d)
(e)
30Hf
35Hf
40Hf
45Hf
50Hf

Figure 13

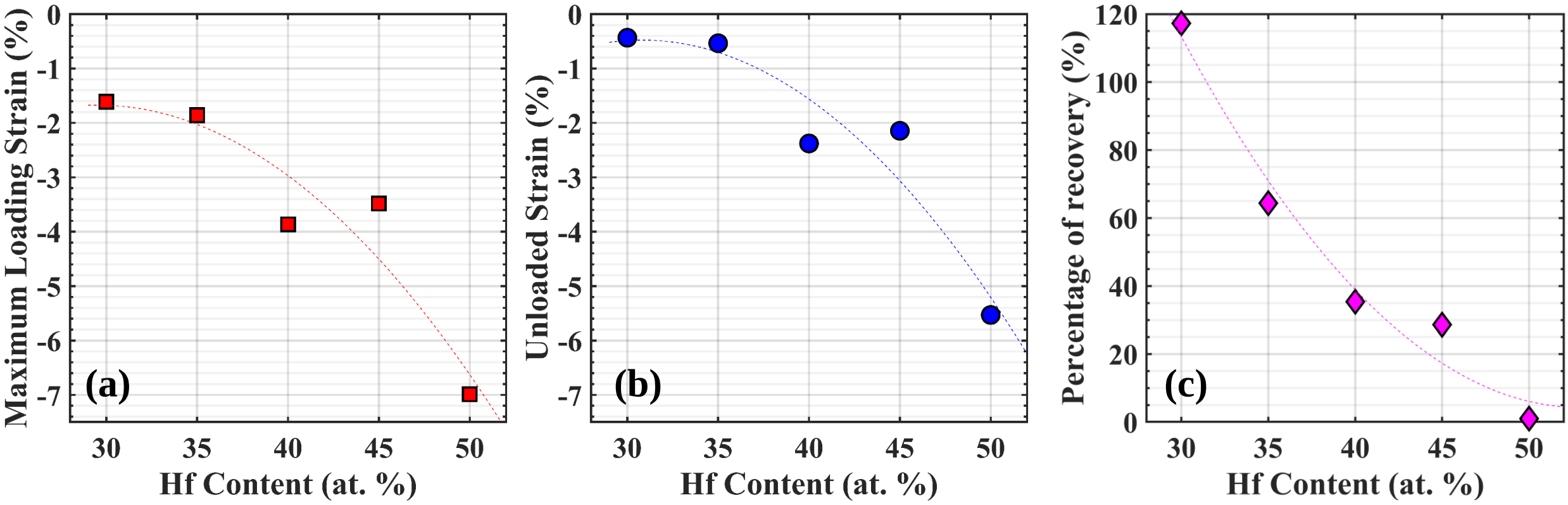
Maximum Loading Strain (%)
0
-1
-2
-3
-4
-5
-6
-7
(a)
30
35
40
45
50
Hf Content (at. %)
Unloaded Strain (%)
0
-1
-2
-3
-4
-5
-6
-7
(b)
30
35
40
45
50
Hf Content (at. %)
Percentage of recovery (%)
120
100
80
60
40
20
0
(c)
30
35
40
45
50
Hf Content (at. %)

Figure 14

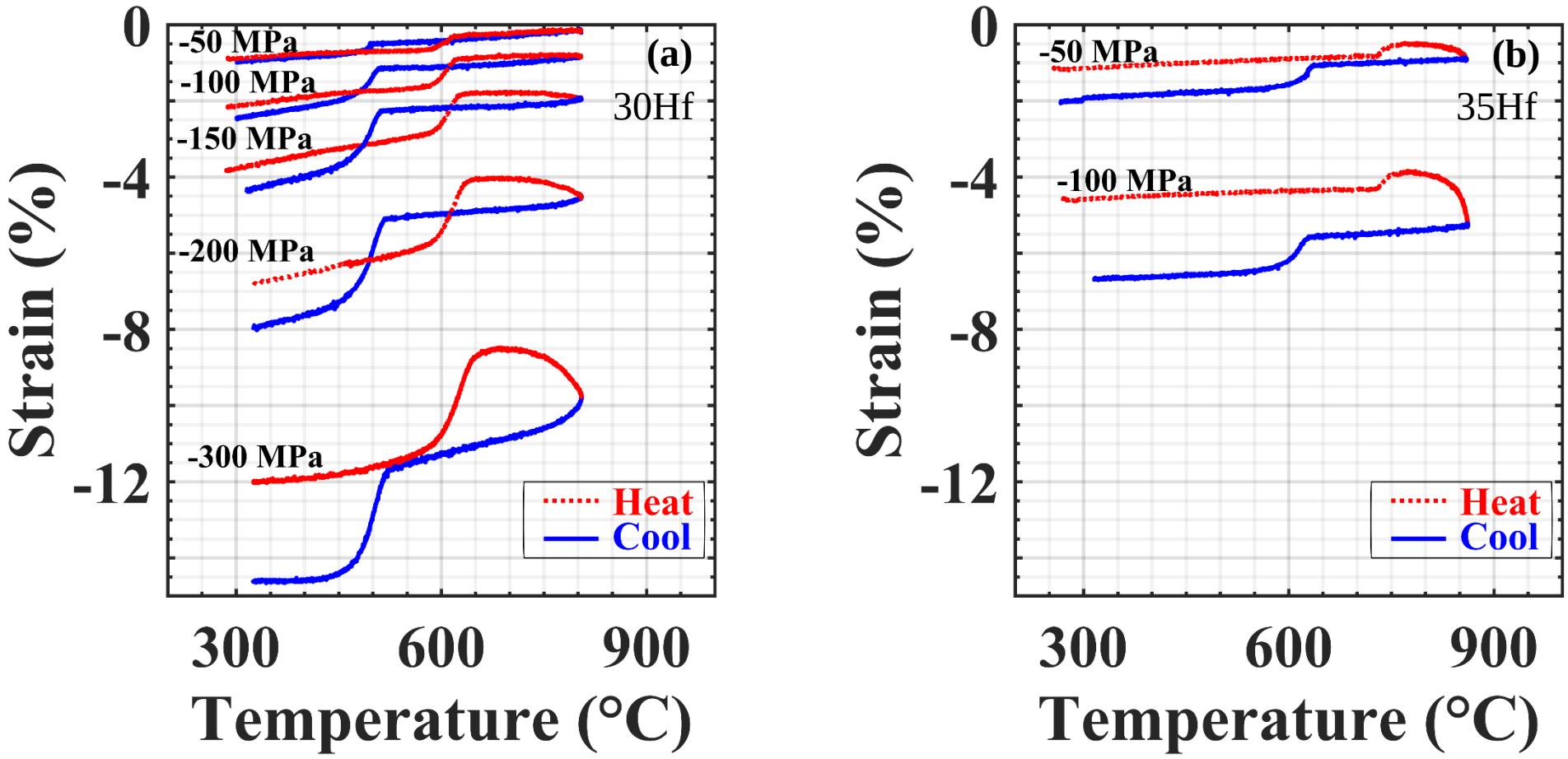
0
-4
-8
-12
Strain (%)
-50 MPa
-100 MPa
-150 MPa
-200 MPa
-300 MPa
(a)
30Hf
Heat
Cool
300
600
900
Temperature (°C)
0
-4
-8
-12
Strain (%)
-50 MPa
-100 MPa
(b)
35Hf
Heat
Cool
300
600
900
Temperature (°C)

Reference	Material Form or Process	Hf (at.%)	Ni (at.%)																
			40	45	46.1	46.8	48	48.5	49	49.2	49.3	49.4	49.7	49.8	50	50.1	50.3	51	51.2
Tong [15]	Thin Film	23		NR															
Bucsek [22]	Ingot (VIM)	24.1															B19'		
Sanjabi [13], Muir Wood [14]	Thin Film	24.4									NR								
Abuzaid [20]	Single crystal	24.7															B19'		
Sehitoglu [21]	Single crystal	24.7															B19' / B19		
Pu [7]	Ingot (VIM)	25						B19											
AbuJudom [5]	Buttons (VAM)	25							NR										
Zhu [8]	Sheet (VIM)	25						B19											
Gao (1997)	VIM	25					B19'												
Santamarta [17]	Rods (VIM)	25														B19'			
Umale [23]	Buttons (VAM)	25												B19'			B19'		
Potapov [10]	Ribbon	25												B19'					
Wu [9]	Sheet (VIM)	25.1			B19														
Patriarca [18]	PAM	25.4																	B19
Gu [11]	Thin Film	26.2											NR						
Sanjabi [13], Muir Wood [14]	Thin Film	28.7								NR									
Gu [11]	Thin Film	29.9										NR							
Wu [9]	Sheet (VIM)	29.9				B19													
AbuJudom [5]	Buttons (VAM)	30							NR										
Zhu [8]	Sheet (VIM)	30						B19											
Umale [23]	Buttons (VAM)	30												B19'			B19'		
Rao [16]	Thin Film	30	B19'/ R																
Kang [12]	PAM	30													B19				
Semenova [28]	VAM	30													B33				
Yeremenko [24]	VAM	30													B33				
Ross [29]	VAM	50													B33				

Table 1: A summary of previous works documenting NiTiHf alloys with Hf content above 20 at.% and their reported phase structures. NR = Not reported; VIM = Vacuum induction melting; VAM = Vacuum arc melting; PAM = Plasma arc melting.

Alloy (at.%)	Transformation Temperatures (°C)						*Hysteresis (A_f - M_s)*
	A_s	A_p	A_f	M_f	M_p	M_s	(°C)
$Ni_{50}Ti_{20}Hf_{30}$	580	608	632	340	419	431	201
$Ni_{50}Ti_{15}Hf_{35}$	724	748	781	490	565	607	174
$Ni_{50}Ti_{10}Hf_{40}$	843	896	984	648	728	758	226
$Ni_{50}Ti_{5}Hf_{45}$	992	1049	1071	824	866	893	178
$Ni_{50}Ti_{0}Hf_{50}$	1149	1160	1190	1097	1118	1148	42

Table 2: Transformation temperatures measured by DSC, and the calculated thermal hysteresis for each alloy.

Alloy (at.%)	Lattice parameters (Orthorhombic B33)			
	***a* (Å)**	***b* (Å)**	***c* (Å)**	
$Ni_{50}Ti_{20}Hf_{30}$	3.105	9.598	4.08	This work
$Ni_{50}Ti_{15}Hf_{35}$	3.115	9.603	4.08	
$Ni_{50}Ti_{10}Hf_{40}$	3.151	9.634	4.092	
$Ni_{50}Ti_{5}Hf_{45}$	3.192	9.736	4.095	
$Ni_{50}Hf_{50}$	3.202	9.758	4.095	
	3.21	9.99	4.1	Yeremenko et al. [24]
	3.22	9.82	4.12	Nash et al. [27]
	3.218	9.788	4.117	Gupta [25]

Table 3: Measured lattice parameters for the B33 phase at room temperature.